Lattice Boltzmann method for simulation of diffusion magnetic resonance imaging physics in heterogeneous tissue models

Noel M. Naughton [1, 2], Caroline G. Tennyson[3], John G. Georgiadis[1,2,4*]

[1]*Mechanical Science & Engineering Department, University of Illinois at Urbana-Champaign, Urbana, IL 61801, USA*
[2]*Beckman Institute For Advanced Science and Technology, Urbana, IL 61801, USA*
[3] *Schlumberger Technology Corporation, Houston, Texas 77041, USA*
[4] *Biomedical Engineering Department, Illinois Institute of Technology, Chicago, IL 60616, USA*

*Corresponding author

Email addresses: nnaught2@illinois.edu (N. M. Naughton), carolinegtennyson@gmail.com (C. G. Tennyson), jgeorgia@iit.edu (J.G. Georgiadis)

ABSTRACT

We report the first implementation of the Lattice Boltzmann method (LBM) to integrate the Bloch-Torrey equation, which describes the evolution of the transverse magnetization vector and the fate of the signal of diffusion magnetic resonance imaging (dMRI). Motivated by the need to interpret dMRI experiments on skeletal muscle, and to offset the small time step limitation of classical LBM, a hybrid LBM scheme is introduced and implemented to solve the Bloch-Torrey equation in a tissue model consisting of cylindrical inclusions (representing bundles of parallel myocytes), delineated by thin permeable membranes (sarcolemma) and surrounded by a extracellular domain (endomysium). As implemented, the hybrid LBM scheme accommodates piece-wise uniform transport, dMRI parameters, periodic outer boundary conditions, and finite membrane permeabilities on non-boundary-conforming inner boundaries. The geometry is discretized in uniform 2D or 3D lattices by locating the curved cylindrical boundaries halfway between lattice nodes. By comparing with analytical solutions of limiting cases, we demonstrate that the hybrid LBM scheme is more accurate that the classical LBM scheme. The proposed explicit LBM scheme maintains second-order spatial accuracy, stability, and first-order temporal accuracy for a wide range of parameters. The parallel implementation of the hybrid LBM code in a multi-CPU computer system with MPI is straightforward. For a domain decomposition algorithm on one million lattice nodes, the speedup is linear up to 168 MPI processes. While offering certain advantages over finite element or Monte Carlo schemes, the proposed hybrid LBM constitutes a sui generis scheme that can by easily adapted to model more complex interfacial conditions and physics in heterogeneous multiphase tissue models, and to accommodate sophisticated dMRI sequences.

Keywords: Bloch-Torrey equation; Lattice Boltzmann method; parallel computation, truncation error; diffusion magnetic resonance imaging; heterogeneous tissue model, skeletal muscle; myocyte; membrane permeability

1. Introduction

Random molecular motion in the presence of tailored magnetic field gradients impart a phase dispersion in the nuclear spin transverse magnetization, and the resulting signal loss has been employed to quantify the statistics of that motion and probe microscopic diffusion barriers in heterogeneous media [1]. The present work is motivated by the need to interpret this signal during water diffusion through heterogeneous biological tissues, which are here exemplified by skeletal muscle tissue. Starting with an early experiment using proton-NMR [2], diffusion magnetic resonance imaging (dMRI) techniques have been used to probe skeletal muscle, both microscopically [3] and macroscopically [4-7]. A growing body of muscle dMRI applications [8] parallels the explosive use of dMRI of human brain [9], but it has not yet reached the sophistication of high resolution imaging of the Human Connectome project [10]. Setting aside issues related to MR instrumentation or the logistics of imaging active muscle in-vivo, one of the areas that muscle dMRI lags behind brain dMRI is in the physical interpretation of the results. A rational method to interpret all dMRI results systematically is to employ (sub-voxel) tissue models that can accommodate both proton-MR physics and microstructural information [11]. This interpretation involves the coupling of dMRI sequences with a solution of the following inverse problem [12]: given the dMRI signal, extract local cellular structure and mass transport properties. Most of the challenges involve the modeling of the tissue microstructure, which typically contains multiple diffusion barriers and a heterogeneous distribution of transport and MRI parameters. Despite the fact that brain and muscle tissues are both characterized by unidirectional fiber microstructures (bundles of neurons and fascicles of myocytes, respectively), there are important differences that prevent the direct translation of dMRI models from brain to muscle: myocyte diameters are an order of magnitude larger than that of neurons, their intracellular morphology is more complex (sarcoplasmic reticulum network), and their membrane (sarcolemma) is more permeable to water than (white matter) neurons, which are bounded by lipid-based (myelin) sheaths. Although MR physics remains the same, diffusion lengths are longer and water transport barriers are more complicated in muscle. Additionally, the hierarchical structure of muscle spans longer length scales than in white matter [13]. The presence of adipose tissue infiltration in muscle complicates both the tissue modeling [14] and imaging [15] aspects of dMRI. These differences necessitate the careful development of numerical dMRI models for muscle, which can be potentially applied to brain dMRI as well.

Although many reduced dMRI models have been employed based on limiting cases [11], a-priori Brownian motion statistics [16] or parameterized effective medium models [17-19], our focus here remains on continuum models based on realistic representations of individual cell geometry and tissue microstructure, which are contained in tissue-based representative elementary volumes (REV). These are typically coupled to the Bloch-Torrey partial differential equation, which is a semi-classical model describing the evolution of bulk magnetization of spin ensemble in space and time [20]. This equation can accommodate spin ensemble physics by modeling the effect of externally applied magnetic field gradients (whose timing defines the dMRI sequence), diffusion, and bulk flow. Such continuum models are useful in at least two ways: (i) given a microscopic reconstruction of the tissue microstructure (a tissue model), simulate the signal from a given dMRI experiment on it (the forward problem), or (ii) develop more accurate reduced dMRI models to solve the inverse problem, especially for muscle tissue. The literature up to 2001 has been summarized in [11], and more recently in [21], again with emphasis on white-matter tissue models. It is worth mentioning in passing, that a modified Bloch-Torrey equation based on fractional space and time derivatives has been introduced to model anomalous water diffusion in the human

brain[22]; such models are a subset of a wider class of fractional calculus models employed in a variety of biological phenomena[23].

The objective of the present work is to revisit and develop a novel simulation method for the forward problem, which involves the numerical integration of the Bloch-Torrey equation in a specified tissue-based continuum REV. The Bloch-Torrey partial differential equation is a linear diffusion-reaction equation, with a reaction term that is a linear function of space and a function of time. The numerical methodologies applied to the solution of Bloch-Torrey equation can be classified in terms of the schemes applied in the discretization of the diffusion operator. These numerical schemes are based on Monte Carlo [24-29], finite difference [30-33] and finite element [34-36] methods. The majority of the schemes employ the forward-Euler temporal discretization [24] of the Bloch-Torrey reaction term, which is first order in time. Higher order temporal discretization schemes using finite elements have been introduced recently, such as an explicit Runge-Kutta [34, 37] and a second-order implicit scheme based on Crank-Nicolson [35, 36]. Based on boundary-conforming finite elements, these schemes have definite advantages over finite differences in terms of describing complex boundaries. This advantage is shared with Monte Carlo methods, which are very simple to code but require careful optimization in order to run efficiently [38, 39].

To our knowledge, there are no prior archival publications describing the use and analysis of the Lattice Boltzmann method (LBM) applied to the solution of the Bloch-Torrey equation. As a mesoscopic method based on the discrete Boltzmann equation, LBM is particularly efficient for simulating transport processes in complex heterogeneous biological tissue, whereby each lattice node can be assigned unique physics or transport properties. LBM is competitive relative to other computational methods because it involves uncomplicated algorithms, handles complex boundary conditions efficiently and accurately [40, 41, 42 , 43], and is naturally amenable to parallelization [44-46]. Some of the challenges of LBM is the constraint it imposes on the time step (typical of explicit schemes), and the requirement to derive special boundary conditions for the probability distribution functions in order to preserve the consistency and accuracy of the numerical scheme [40, 47].

This work introduces a hybrid implementation of the LBM to integrate the Bloch-Torrey equation in heterogeneous tissue models, which carries the following advantages

- Obviates the problem of the classical LBM implementations, which require small temporal steps when applied to reaction-diffusion problems with dominant reaction terms.
- Retains the second-order spatial accuracy in multi-compartmental domains containing complex permeable interfaces.
- The numerical algorithm can be easily parallelized and executed efficiently with high parallel efficiency in multi-core computer systems. Based on spatial domain decomposition, the expectation is that the kinetic nature of the LBM and the locality of the operations involved result in execution times that scale linearly with the number of cores.

Although the development of the hybrid LBM scheme (described in the following) is motivated by the need to interpret the dMRI signal in muscle tissue, the overarching aim of this work is to support the claim that the proposed scheme is accurate, fast, and can accommodate complex geometries of relevance to more general tissue models.
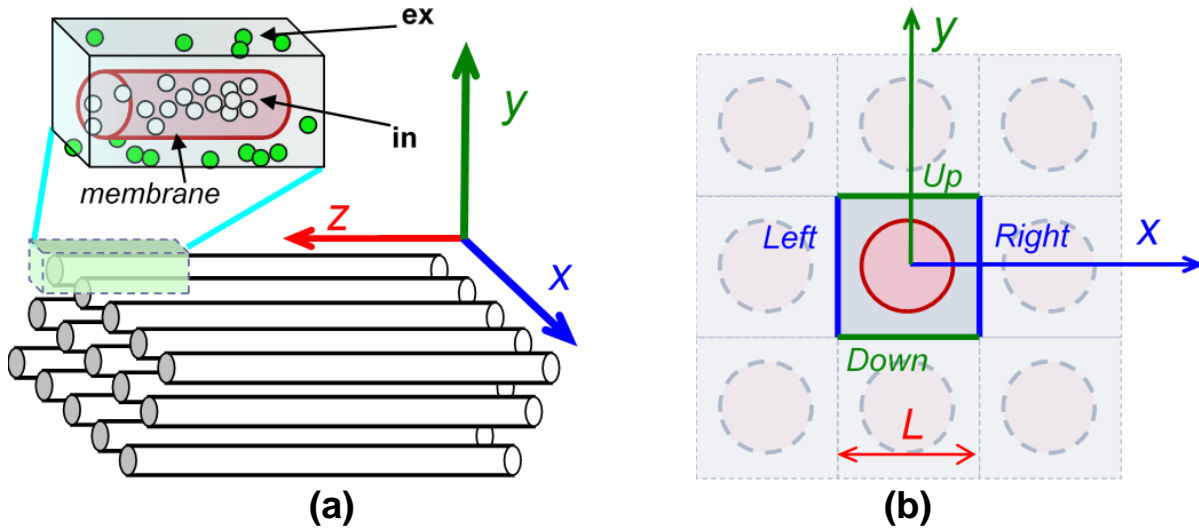
Figure 1. (a) Periodic parallel fiber model of heterogeneous tissue, with intracellular (in) and extracellular (ex) compartments and membrane of infinitesimal thickness. (b) Two-dimensional periodic computational domain and representative elementary volume (REV) of size L.

2. Methods

2.1 Diffusion Weighted Imaging

The governing equation describing proton (^{1}H) spin dynamics in the presence of diffusion during an MRI experiment is the Bloch-Torrey equation [20]. Neglecting coherent (advective) fluid transport, the Bloch-Torrey differential equation can be formulated in a coordinate frame rotating at a fixed Larmor frequency (determined by the MR scanner permanent magnetic field) as follows:

$$\frac{\partial \boldsymbol{M}}{\partial t} = -j\,\gamma[\boldsymbol{x} \cdot \boldsymbol{G}(t)]\boldsymbol{M} - \frac{\boldsymbol{M}}{T_2} + \nabla \cdot (D(\boldsymbol{x})\nabla \boldsymbol{M}) \,; \quad \boldsymbol{M}(\boldsymbol{x},t) = ReM(\boldsymbol{x},t) + j\,ImM(\boldsymbol{x},t) \quad (1)$$

where $\boldsymbol{M}(\boldsymbol{x},t)$ is a complex variable representing the bulk (transverse) magnetization of the spins, j is the imaginary unit, γ is the gyromagnetic ratio for ^{1}H, $\boldsymbol{x}$ is the spin position vector, $\boldsymbol{G}(t)$ is the time-varying magnetic field gradient vector used to encode diffusion, T_2 is the spin-spin relaxation time, and D is the diffusion coefficient. Except for γ, all the variables listed above are local, in that they represent the ensemble average of spin behavior at a given spatial location. For definiteness, the spatial domain considered for the forward problem corresponds to heterogeneous tissues consisting of a matrix surrounding fibrous inclusions, cf. Figure 1(a). The Bloch-Torrey equation is solved here in a representative elementary volume (REV) containing intracellular (in) and extracellular (ex) subdomains, cf. Figure 1(b). Furthermore, we will consider problems with isotropic diffusion and piece-wise uniform T_2 and D. Referring to the two subdomains in Figure 1(b), for example, there are two diffusion coefficients, D_{in} and D_{ex}, for intracellular and extracellular compartments, respectively. This property notation will be suppressed in the following, until it is explicitly reinstated. The forward problem described by (1) is supplemented with an initial condition $\boldsymbol{M}(\boldsymbol{x},0)$ and appropriate boundary conditions on the REV, which will be

discussed in section 2.3. Decomposing the transverse magnetization $M(x, t)$ as shown in (1), the Bloch-Torrey equation yields two coupled reaction-diffusion equations for $ReM(x, t)$ and $ImM(x, t)$, respectively. The coupling occurs through the first term of the right-hand side of (1), which depends on the specific dMRI sequence.
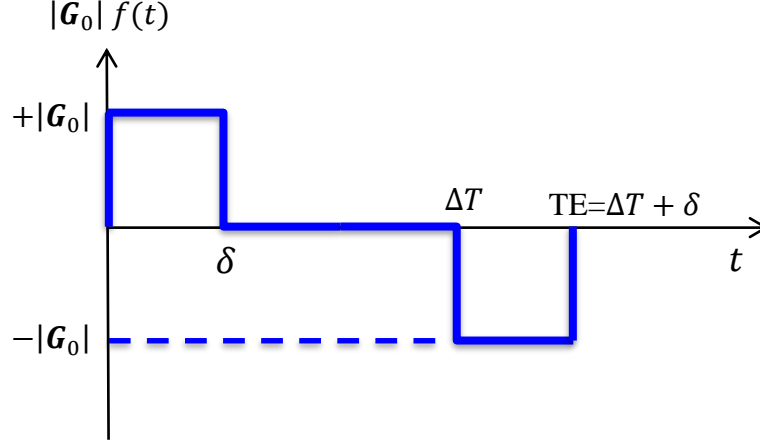

Figure 2. Two-pulse Stejskal-Tanner PGSE sequence with rectangular bipolar gradient waveforms for diffusion MRI.

A typical dMRI sequence is the Stejskal-Tanner Pulse-Gradient-Spin-Echo (PGSE) sequence. Although more sophisticated sequences are in use, we will employ PGSE here since it is adequate to represent MR physics and to study local diffusion without image formation. This sequence involves a bipolar magnetic gradient pulse (diffusion gradients), with the gradient vector $G(t)$ controlled by the operator, cf. Figure 2. The gradient magnitude is typically constant in space but varies in time, so it is convenient to express it in separable form, $G(t) = G_0 f(t)$. By choosing judiciously a set of vectors G_0, each oriented along a specific direction, the signal can be sensitized to probe the dynamics of diffusion along these directions. The timing and strength of these diffusion gradient pulses determines the spatial and temporal variation of the quantity inside the parenthesis of the first term on the right hand side of (1). The resulting evolution of $M(x, t)$ generates a time-varying magnetic flux in the scanner receiver and induces a voltage variation in the receiver coil. This voltage variation constitutes the dMRI signal, which is acquired upon the appearance of a "spin echo" at time $t = TE$. Assuming spatially uniform spin density, the dMRI signal S is obtained by averaging $|M|$ over the representative elementary volume (REV), for each $G(t)$. In addition to the gradient orientation, three parameters are used to describe the diffusion gradient pair in PGSE: the diffusion gradient amplitude $|G_0|$ (along a given direction), gradient pulse duration δ, and delay ΔT between the gradient pulses, cf. Figure 2. These parameters are grouped in the definition of the diffusion decay factor

$$b = \gamma^2 \int_0^{TE} \left(\int_0^{t'} G(t'')dt'' \right)^2 dt' = \gamma^2 \int_0^{TE} \left(G_0 \int_0^{t'} f(t'')dt'' \right)^2 dt' = \gamma^2 |G_0|^2 \delta^2 (\Delta T - \delta/3) \quad (2)$$

The final expression in (2) is valid for the PGSE sequence only. An apparent diffusion coefficient (ADC) can be estimated along the direction of each diffusion gradient G_0 from the ratio:

$$\ln\left(\frac{S}{S_0}\right) = -b\ (ADC), \quad (3)$$

where S is the signal at $t = TE$ for a finite $\boldsymbol{G}_0$, and S_0 is the signal for $\boldsymbol{G}_0 = 0$, both averaged over the REV. In the case of unrestricted diffusion in a (homogeneous) medium with a diffusion coefficient D, an asymptotic analysis [12] at the short pulse limit ($\delta \ll \Delta T$) shows that $ADC = D$. Practical implementation of dMRI to estimate ADC involves measuring S, S_0 and then using equation (3); this implies that typical b-values are chosen so that $b\, D \sim O(1)$.

2.2 Hybrid Lattice Boltzmann method

An order of magnitude analysis of the terms of the right hand side of (1) is presented in Appendix A for typical simulations of dMRI experiments. The phase of the magnetization vector $\boldsymbol{M}(x, y, t)$ exhibits fast oscillations when the term $\boldsymbol{x} \cdot \boldsymbol{G}(t)$ becomes large. As the truncation error analysis in Appendix A shows, the implementation of the classical LBM method to solve the reaction diffusion equation (1) introduces a truncation error term that grows with the square of the REV length size. Instead, a hybrid Lattice Boltzmann method involving the factorization of the operator in terms of a reaction (fast), and a diffusion (slow) operator is introduced here

$$\boldsymbol{M}(\boldsymbol{x}, t) = \exp\left[-j\ \gamma[\boldsymbol{x} \cdot \boldsymbol{G}(t)]\ \delta t' - \frac{1}{T_2}\delta t'\right]\boldsymbol{M}'(\boldsymbol{x}, t) \qquad (4)$$

where $\boldsymbol{M}'(\boldsymbol{x}, t)$ is an intermediate function. The exponent in (4), with $\delta t'$ denoting the reaction time step (employed in the discretization of the reaction term), has been reported first in [24] and has since been used in most schemes [25-32] to integrate the Bloch-Torrey equation. As shown in Appendix A, this functional form of the exponent is appropriate for $\boldsymbol{G}(t)$ piece-wise constant in time, like in the case of the PGSE gradient pulse sequence, cf. Figure 2. For sequences with gradient pulses of different time-dependence, we also show how it can be generalized. Equation (1) is recovered from (4), accurate to first order in $\delta t'$ (Appendix A), if $\boldsymbol{M}'$ obeys the following diffusion equation

$$\frac{\partial \boldsymbol{M}'}{\partial t} = \nabla \cdot (D\nabla \boldsymbol{M}') \qquad (5)$$

Equation (5) is integrated with the classical LBM algorithm over a diffusion time step δt, as shown below. The proposed hybrid LBM for the integration of (1) is essentially a time splitting scheme:

$$\left.\begin{array}{c}\text{Diffusion split during } [t, t + \delta t]: \quad \boldsymbol{M}(\boldsymbol{x}, t) \to \bar{\boldsymbol{M}}(\boldsymbol{x}, t + \delta t) \text{ from Eq. (5)},\\ \text{then, initialize } \boldsymbol{M}'(\boldsymbol{x}, t) = \bar{\boldsymbol{M}}(\boldsymbol{x}, t + \delta t), \text{and}\\ \text{Reaction split during } [t, t + \delta t']: \quad \boldsymbol{M}'(\boldsymbol{x}, t) \to \boldsymbol{M}(\boldsymbol{x}, t + \delta t') \text{ from Eq. (4)}\end{array}\right\} \quad (6)$$

As written, the practical implementation of the time splitting scheme (6) requires that the diffusion and reaction time steps are identical ($\delta t = \delta t'$), but this is not necessary. In fact, one of the advantages of separating diffusion and reaction steps is that different time steps or time-splittig schemes [48] can be used depending on the stiffness of the equations (4-5). For example, one can use $\delta t = k\ \delta t'$, with an integer $k > 1$, solve Eq. (5) for 1 step, and then solve Eq. (4) for k steps so that the timing is consistent. As the analysis in Appendix A indicates, $\delta t = \delta t'$ is a choice that is consistent with the range of physical and numerical parameters pertinent to the present work. In the following and unless explicitly specified otherwise, when we refer to the time step, $\delta t = \delta t'$ is assumed.

The integration of (5) during the diffusion split is performed with the classical LBM algorithm. The most common version is based on a single relaxation parameter (Bhatnagar–Gross–Krook model) and can be expressed as:

$$g_i(x + \delta x \, e_i, t + \delta t) - g_i(x, t) = -\frac{1}{\tau}\left[g_i(x, t) - g_i^{eq}(x, t)\right] \qquad (7)$$

where g_i is the particle probability distribution function defined on a discrete lattice, i denotes the lattice direction, x is the space coordinate on the lattice, δx is the lattice spacing (grid size), e_i is the lattice (speed) vector, δt is the diffusion time step, g_i^{eq} is an equilibrium state for g_i, and τ is the dimensionless relaxation time. Like the magnetization M, the function g_i is a complex variable. Since the zero-th moment of g_i is equal to M, the magnetization vector components are recovered by taking the sum of these functions over the lattice directions. Following the Chapman-Enskog analysis of (7), the diffusion equation (5) can be recovered, accurate to $O(\delta t, \delta x^2)$, if the relaxation time parameter τ is defined as

$$\tau = \frac{1}{2} + \frac{\delta t}{\varepsilon_D (\delta x)^2} D \qquad (8)$$

where ε_D is a positive constant (a free parameter) equal to the ratio of the speed of sound squared over the lattice speed squared $(\delta x / \delta t)^2$. The relaxation time τ depends on the diffusion coefficient D, which is a fixed physical parameter and therefore independent of the time step δt and grid size δx. Because advection is neglected, the equilibrium distribution function for the LBM scheme (irrespective of whether the reaction term is included) is given by

$$g_i^{eq}(x, t) = \omega_i \, M(x, t) \qquad (9)$$

where ω_i are appropriate weighting factors that are consistent with the LBM lattice topology and the value of ε_D.
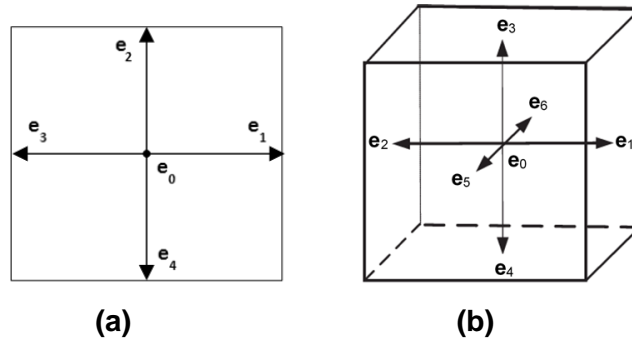

Figure 3. Stencils for Lattice Boltzmann scheme. **(a)** two-dimensional, five-speed (D2Q5) and **(b)** three-dimensional, seven-speed (D3Q7).

The theoretical development reported in this section is confined to 2-D isotropic diffusion, thus a 2-D square lattice, 5-speed model (D2Q5), as shown in Figure 3, has sufficient symmetries for a consistent spatial discretization of (5). In fact, an analysis of the 2-D advection-diffusion equation [49] indicates that the D2Q5 stencil produces more accurate and robust results than D2Q9, which is the 9-speed stencil.

The D2Q5 lattice speed vectors in (7) are given by

$$\mathbf{e}_i = \begin{cases} (0,0) & (i = 0) \\ (\pm 1, 0), (0, \pm 1) & (i = 1,2,3,4) \end{cases} \qquad (10)$$

Here we set $\varepsilon_D = \frac{1}{3}$. The weighting factors for the equilibrium distribution become [50]

$$\omega_i = \begin{cases} \varepsilon_D & (i = 0) \\ \dfrac{\varepsilon_D}{2} & (i = 1,2,3,4) \end{cases} \qquad (11)$$

Under the classical LBM scheme, the evolution equation (7) is integrated in two steps over δt, a collision step ($\boldsymbol{g}_i \to \hat{\boldsymbol{g}}_i$) followed by a streaming step ($\hat{\boldsymbol{g}}_i \to \bar{\boldsymbol{g}}_i$). The collision step is

$$\hat{\boldsymbol{g}}_i(\boldsymbol{x}, t) = \boldsymbol{g}_i(\boldsymbol{x}, t) - \frac{1}{\tau}\big[\boldsymbol{g}_i(\boldsymbol{x}, t) - \boldsymbol{g}_i^{eq}(\boldsymbol{x}, t)\big] \qquad (12)$$

where $\boldsymbol{g}_i$ is the initial particle distribution at the beginning of the time step, $\boldsymbol{g}_i^{eq}$ is the equilibrium particle distribution (9), and $\hat{\boldsymbol{g}}_i$ is the particle distribution function following the collision step, which is the input to the streaming step. The streaming step is

$$\bar{\boldsymbol{g}}_i\left(\boldsymbol{x} + \delta x\, \boldsymbol{e}_i, t + \delta t\right) = \hat{\boldsymbol{g}}_i(\boldsymbol{x}, t) \qquad (13)$$

From here the reaction step is initialized as $\boldsymbol{g}_i'(\boldsymbol{x}_n, t^k) = \bar{\boldsymbol{g}}_i(\boldsymbol{x}_n, t^{k+1})$, where $t^k = k\, \delta t'$. The magnetization vector $\boldsymbol{M}'(\boldsymbol{x}, t)$ is computed by the zero-th moment of the particle probability distribution function (sum over the lattice speed vectors) as follows

$$\boldsymbol{M}'(\boldsymbol{x}, t) = \sum_{i=0}^{4} \boldsymbol{g}_i'(\boldsymbol{x}, t) \qquad (14)$$

As proven in [50], the above LBM scheme is unconditionally stable for $\tau > 1/2$, which is always satisfied given that D in the expression (8) is positive.

The integration (4) during the reaction split accounts for the effects of the diffusion gradient pulse and T_2 relaxation on the magnetization. We start with a discretized version of (4)

$$\boldsymbol{M}(\boldsymbol{x}_n, t^k + \delta t') = \exp(-j\, \gamma\, [\boldsymbol{x}_n \cdot \boldsymbol{G}(t^k)]\delta t')\, \exp(-\delta t'/T_2)\, \boldsymbol{M}'(\boldsymbol{x}_n, t^k) \qquad (15)$$

where $\boldsymbol{x}_n$ denotes the coordinate location, and $\boldsymbol{G}(t^k) = \boldsymbol{G}_0\, f(t^k)$ is the gradient vector at time t^k. By substituting (14) into (15), the distribution function after the completion of the reaction step at $t^{k+1} = t^k + \delta t'$ becomes

$$\boldsymbol{g}_i(\boldsymbol{x}_n, t^{k+1}) = \exp(-j\, \gamma[\boldsymbol{x}_n \cdot \boldsymbol{G}_0]f(t^k)\delta t')\, \exp(-\delta t'/T_2)\, \boldsymbol{g}_i'(\boldsymbol{x}_n, t^k) \qquad (16)$$

The hybrid LBM scheme is summarized below in terms of the sequence of the particle distribution functions ($\boldsymbol{g}_i \to \hat{\boldsymbol{g}}_i \to \boldsymbol{g}_i' \to \bar{\boldsymbol{g}}_i$) computed at each step

$$\left.\begin{array}{lll} \text{Collision at } t^k: & \boldsymbol{g}_i(\boldsymbol{x}_n, t^k) \to \hat{\boldsymbol{g}}_i(\boldsymbol{x}_n, t^k), & \text{Eq. (12);} \\ \text{Streaming at } t^k: & \hat{\boldsymbol{g}}_i(\boldsymbol{x}_n, t^k) \to \bar{\boldsymbol{g}}_i(\boldsymbol{x}_n + \delta x\, \boldsymbol{e}_i, t^{k+1}), & \text{Eq. (13);} \\ \multicolumn{2}{l}{\quad \text{then, initialize } \boldsymbol{g}_i'(\boldsymbol{x}_n, t^k) = \bar{\boldsymbol{g}}_i(\boldsymbol{x}_n, t^{k+1}).} & \\ & & \\ \text{Reaction at } t^k: & \boldsymbol{g}_i'(\boldsymbol{x}_n, t^k) \to \boldsymbol{g}_i(\boldsymbol{x}_n, t^{k+1}), & \text{Eq. (16)} \end{array}\right\} \quad (17)$$

The phase in the first term on the right hand side of (16), which is a function of space and time, couples the computation of the distribution functions. Assume, for example, that a diffusion gradient $\boldsymbol{G}_0$ is applied in the (x, y) plane, and there are $[N + 1] \times [N + 1]$ lattice nodes in 2D the REV shown in Figure 1(b). The phase in (16) at time t^k and location $\boldsymbol{x}_n$ becomes,

$$\Delta\varphi_n^k = \gamma[\boldsymbol{x}_n \cdot \boldsymbol{G}_0]f(t^k)\delta t', \quad \text{with} \quad n \in [0,1,2,\dots N] \times [0,1,2,\dots N] \quad (18)$$

In the current implementation of the LBM code, the distribution function $\boldsymbol{g}_i$ is then updated in terms of its real ($Re\boldsymbol{g}_i$) and imaginary ($Im\boldsymbol{g}_i$) components, as follows

$$
\begin{aligned}
Re\boldsymbol{g}_i(\boldsymbol{x}_n, t^{k+1}) &= [Re\boldsymbol{g}_i'(\boldsymbol{x}_n, t^k)\cos(\Delta\varphi_n^k) - Im\boldsymbol{g}_i'(\boldsymbol{x}_n, t^k)\sin(\Delta\varphi_n^k)]\exp(-\delta t'/T_2) \\
Im\boldsymbol{g}_i(\boldsymbol{x}_n, t^{k+1}) &= [Im\boldsymbol{g}_i'(\boldsymbol{x}_n, t^k)\cos(\Delta\varphi_n^k) + Re\boldsymbol{g}_i'(\boldsymbol{x}_n, t^k)\sin(\Delta\varphi_n^k)]\exp(-\delta t'/T_2)
\end{aligned}
\quad (19)
$$

For simplicity, the bold font notation for $\boldsymbol{g}_i$ and the other sequence members is henceforth suppressed.

2.3 Boundary Conditions

In the following, we show how the boundary conditions are expressed in terms of the distribution functions for external boundaries, which are periodic, and internal boundaries consisting of the mathematically membranes separating the "in" from "ex" subdomains.

2.3.1 Modified periodic boundary condition

The typical method to terminate the prescribed external boundary conditions for the REV in 2D is to consider an infinite periodic solution domain exhibiting a spatial translation symmetry along *x* and *y*, as shown in Figure 1(b). Given the linear spatial dependence of the signal phase, owing to the dMRI gradient term $[\boldsymbol{x} \cdot \boldsymbol{G}_0 \, f(t)]$ in Eq. (1), conventional periodic conditions do not apply. Let us consider a spatial period L (size of the REV), and the two (vertical) boundaries marked "Left" and "Right" in Figure 1(b). As demonstrated in [32], the magnetization on these boundaries obeys the following constraint

$$\boldsymbol{M}(\boldsymbol{x}_{Left}, t) = \exp[j\,\varphi(L, t)]\,\boldsymbol{M}(\boldsymbol{x}_{Right}, t); \quad \varphi(L, t) = \gamma\left[(\boldsymbol{x}_{Right} - \boldsymbol{x}_{Left}) \cdot \boldsymbol{G}_0\right]\int_0^t f(t')dt' \quad (20)$$

This means that the periodic boundary condition results in a phase difference that is proportional to the component of $\boldsymbol{G}_0$ perpendicular to the boundaries, the spatial period L and an integral factor that varies with time. If $\boldsymbol{G}_0$ is applied only along *x*, then the periodic boundary condition along the two (horizontal) boundaries marked "Up" and "Down" in Figure 1(b) reduces to the conventional form

$$\boldsymbol{M}(\boldsymbol{x}_{Down}, t) = \boldsymbol{M}(\boldsymbol{x}_{Up}, t) \quad (21)$$

To further simplify the presentation, we set $t^k = k\,\delta t$, and keep only *x*-coordinate dependence below, with $x_n = n\,\delta x$, where $n \in [0,1,2,\dots N]$. Since the spatial period is $L = N\,\delta x$, the phase in (20) can be discretized by approximating the integral by a sum (low order approximation is consistent with (A.9))

$$\varphi(L, t^k) = \gamma\,L\,|\boldsymbol{G}_0|\sum_{m=0}^{k-1} f(t^m)\,\delta t \quad (21)$$

A key point is that all boundary conditions are applied between the collision and streaming step. The modified periodic boundary condition has been adapted to the LBM scheme as follows. Two external "buffer" lattice rows are introduced at $n \in [-1, N + 1]$ in order to complete the streaming step at $n = 0$ and $n = N$. The following assignments are applied to these rows after the collision step,

9

$$\hat{g}_i(x_{-1}, t^k) = \exp[j\,\varphi(L, t^k)]\,\hat{g}_i(x_{N-1}, t^k)$$
$$\hat{g}_i(x_{N+1}, t^k) = \exp[-j\,\varphi(L, t^k)]\,\hat{g}_i(x_{\mathbf{1}}, t^k) \tag{22}$$

After the streaming (13) and reaction initialization step, the correct phase difference (21) is maintained for the distributions at the nodes at the "Left" and "Right" boundaries at $n = 0$ and $n = N$, respectively,

$$g_i'(x_0, t^k) = \exp[j\,\varphi(L, t^k)]\,g_i'(x_N, t^k) \tag{23}$$

During the reaction step, each distribution in Eq. (23) gains phase according to Eqs. (16) and (18),
$$g_i(x_0, t^{k+1}) = \exp(-j\,\Delta\varphi_0^k)\exp(-\delta t'/T_2)\,g_i'(x_0, t^k)$$
$$g_i(x_N, t^{k+1}) = \exp(-j\,\Delta\varphi_N^k)\exp(-\delta t'/T_2)\,g_i'(x_N, t^k) \tag{24}$$

Considering Eqs. (18) and (21), it is straightforward to show that

$$\exp(-j\,\Delta\varphi_0^k)\exp[j\,\varphi(L, t^k)]\exp(j\,\Delta\varphi_N^k) = \exp[j\,\varphi(L, t^{k+1})] \tag{25}$$

By incorporating (25), Eqs. (23) and (24) yield
$$g_i(x_0, t^{k+1}) = \exp[j\,\varphi(L, t^{k+1})]\,g_i(x_N, t^{k+1}) \tag{26}$$

which is consistent with the modified periodic boundary condition Eq. (20). This implies that, by making the assignments (22) to the nodes on buffer rows after the collision step, the correct phase difference (21) is maintained for the distributions at the appropriate boundary nodes and at the completion of each time step. For the "Up" and "Down" boundaries, the conventional periodic condition given by Eq (21) is satisfied if we make the following assignment after the collision step:
$$\hat{g}_i(\boldsymbol{x}_{Down}, t^k) = \hat{g}_i(\boldsymbol{x}_{Up}, t^k) \tag{27}$$

2.3.2 Membrane Boundary Condition

Muscle cells are delineated by thin semi-permeable membranes, and like most soft tissues and water, they are weakly diamagnetic, which means that they do not disturb the magnetization significantly. The boundary condition at a thin permeable membrane involves conservation of mass flux of water spins carrying the scalar $\boldsymbol{M}$, without any loss in the membrane. Assuming equal spin density on both sides on the membrane, this implies conservation of magnetization flux across the membrane. Letting $\boldsymbol{n}$ denote the unit vector normal to the membrane and pointing towards the extra-cellular space, and introducing the membrane permeability K, this conservation principle imposes the following boundary condition
$$D_{ex}\boldsymbol{n} \cdot \nabla\boldsymbol{M}_{ex} = D_{in}\boldsymbol{n} \cdot \nabla\boldsymbol{M}_{in} = K(\boldsymbol{M}_{ex} - \boldsymbol{M}_{in}) \tag{28}$$
where $\boldsymbol{M}_{ex}$ and $\boldsymbol{M}_{in}$ denote the values on the extra- and intra-cellular side of the membrane, respectively. The interfacial condition (28), which is a mixed boundary condition, needs to be re-formulated in terms of the particle distribution functions in order to be integrated in the LBM scheme. This is presented in detail in Appendix B, which is based on derivations reported in [42, 51] [52], so only the necessary background is given here. In order to facilitate the presentation,. The boundary condition is applied after the collision step of the LBM algorithm and in place of the streaming step. It is expressed in terms of the distribution functions denoted by $g_i'(\boldsymbol{x}_e, t)$ and

$g_i'(\boldsymbol{x}_f, t)$, respectively, which represent particles going away from the membrane in the extra- and intra-cellular space, cf. Figure B.1, as follows

$$g_i'(\boldsymbol{x}_f, t) = \frac{1}{1+P}\hat{g}_i(\boldsymbol{x}_e, t) + \frac{P}{1+P}\hat{g}_i(\boldsymbol{x}_f, t)$$
$$g_i'(\boldsymbol{x}_e, t) = \frac{P}{1+P}\hat{g}_i(\boldsymbol{x}_e, t) + \frac{1}{1+P}\hat{g}_i(\boldsymbol{x}_f, t) \qquad (29)$$

Here the reaction initialization step is implied. As shown in Appendix B, the membrane permeability in Eq. (28) is introduced directly through the dimensionless parameter P

$$K = \frac{1}{6P}\frac{\delta x}{\delta t} \qquad (30)$$

The membrane boundary conditions (29) describe the particle distribution functions at the end of the streaming step for finite permeability K values and for membrane boundaries located half-way between lattice nodes, i.e., for $\Delta = 0.5$. For the general case of arbitrary $0<\Delta<1$, the distribution functions are determined by solving directly Equations (B.2). We conclude this section with a physical interpretation of the factors in (29) by considering the particle distribution functions involved. The presence of the membrane splits the population of the particles towards the membrane (from either side) into a portion $\frac{1}{1+P}$ that cross and a portion $\frac{P}{1+P}$ that is reflected back. To the limit of infinite permeability ($K \to \infty$ and $P \to 0$), the relationships (29) reduce to Equation (13). This implies that the particle distribution functions $\hat{g}_i$ stream across the membrane (from either side) unaltered, so essentially there is no barrier to diffusion. Conversely, for the limit of impermeability ($K \to 0$ and $P \to \infty$), equation 29 reduces to the standard bounce-back condition for a homogenous Neumann boundary [53].

3. Results

In this section, we first compare the accuracy of the proposed hybrid LBM scheme, summarized by Equation (17), to that of the classical LBM scheme, which is described by replacing equation (12) with expression (A12). All computations involve the numerical integration of the Bloch-Torrey Equation (1) to simulate the evolution of dMRI signal under the PGSE sequence without imaging gradients (Figure 2). This comparison hinges on analytical solutions of the Bloch-Torrey or the diffusion equation (5). Second, we assess the accuracy of the hybrid LBM scheme applied to solve the Bloch-Torrey equation, as a function of spatial resolution, and of the physical and dMRI parameters. Third, we demonstrate the application of the hybrid scheme to simulate the evolution equation in complex spatial domains, and how it scales in a parallel implementation of the computer code under domain decomposition. All the above are performed in 2D, so we conclude this section with a 3D extension of the hybrid LBM scheme, followed by a study of its performance on a parallel computer platform.

Based on the discussion following Equation (6), we will set the time step for the reaction operator identical to that used for the diffusion operator, $\delta t' = \delta t$. The following two dimensionless error estimates are used in the analysis of the computational results. The normalized L2 norm of error between the field grid function $\boldsymbol{M}_N(\boldsymbol{x_n}, t)$ (on a $N \times N$ lattice) and the analytical solution $\boldsymbol{M}(\boldsymbol{x_n}, t)$ is given by

$$\text{L2 error} = \frac{\{\sum_n^{N \times N}[\boldsymbol{M}_N(\boldsymbol{x_n}, t) - \boldsymbol{M}(\boldsymbol{x_n}, t)]^2\}^{\frac{1}{2}}}{\{\sum_n^{N \times N}[\boldsymbol{M}(\boldsymbol{x_n}, t)]^2\}^{\frac{1}{2}}} \qquad (31a)$$

while the relative error between the apparent diffusion coefficient (ADC) computed by (3) and the theoretical value D is defined as
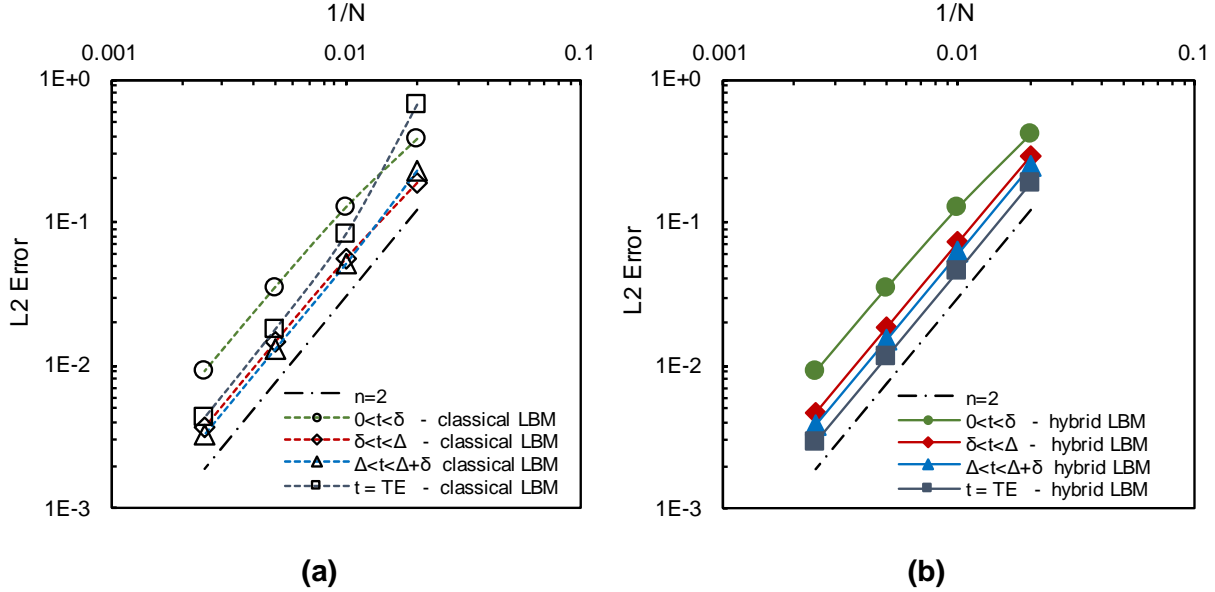
$$\frac{ADC - D}{D} \tag{31b}$$

Figure 4. Grid convergence rate and spatial truncation error of **(a)** classical and **(b)** hybrid LBM schemes, for the impulse response test case, for a 2D square domain ($L = 200\ \mu m$) with $\tau = 0.625$, b = 1000 s/mm^2, δ= 3 ms, ΔT = 6 ms, and TE = 12 ms. The trend line marked with n=2 corresponds to quadratic convergence.

3.1 Comparison of truncation error for classical and hybrid LBM schemes

In this section, we study the truncation error relative to analytical solutions of Equation (1) obtained first with impulse initial condition, and second with uniform initial condition. The predictions of the classical and hybrid LBM schemes were compared to the exact solution of the Bloch-Torrey equation in a periodic domain with uniform diffusion coefficient and subject to an initial Dirac delta distribution $M(x, y, t = 0) = \delta(x, y)$ [34][53]. A square REV with L=200 μm was used, and the remaining physical parameters were b = 1000 s/mm^2, δ = 3 ms, ΔT = 6 ms and TE = 12 ms. The LBM simulations were performed on a $N \times N$ grid for N =50, 100, 200, and 400 lattice points in each direction, and $\tau = 0.625$ was kept fixed. The normalized L2 norms of the errors are plotted in Figure 4 for four time points: $t_1 = \delta/2 = 1.5$ ms, $t_2 = (\Delta T + \delta)/2 = 4.5$ ms, $t_3 = \Delta T + \delta/2 = 7.5$ms, and $t_4 = TE = 12$ms. A trend line corresponding to L2 error $\sim \left(\frac{1}{N}\right)^n$ for $n = 2$ is also included for reference. The results indicate that the spatial convergence of both schemes is second order in space, with the exception of the classical scheme at t_4. In that case, the scheme reaches the asymptotic convergence regime only for grid sizes smaller than $\frac{1}{N} = 0.01$.

In order to highlight the difference between the classical and hybrid LBM scheme as the size L of the domain increases, the numerical solution of the above homogeneous problem was repeated with uniform initial condition $M(x, y, 0) = 1$. The solution is trivial: $M(x, y, t) = \exp(-bD)\exp(-t/T_2)$. The L2 norms of the errors are plotted in Figure 5 as a function of lattice

spacing and time step. For the classical method, the error is given for two domain sizes ($L = 20\ \mu m$, and $L = 100\ \mu m$) to illustrate how the size of the domain (mainly, the size of the source term at the domain edge) affects accuracy. This effect is not manifested for the hybrid scheme. Although both schemes are second order in space, the accuracy of the hybrid scheme is independent of L and higher than that of the classical scheme. Figure 5 indicates that both schemes are first-order accurate in time, as per the discussion in Appendix A.
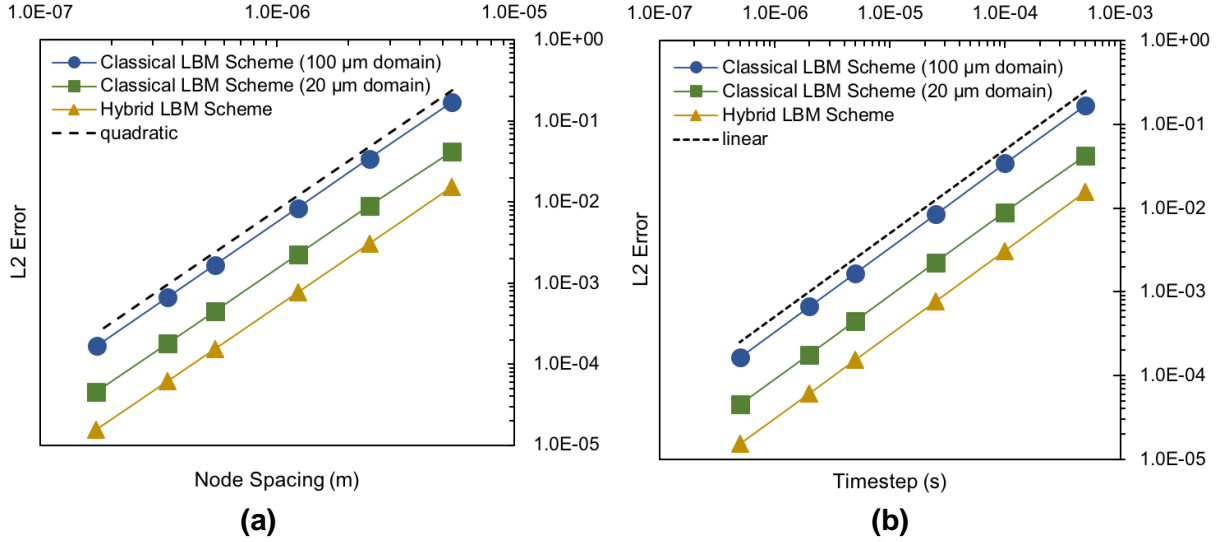
Figure 5. Comparison of spatial **(a)** and temporal **(b)** convergence rates for hybrid and classical LBM schemes for the uniform gradient test case at t=20 ms, with G = 23.16 mT/m and τ = 0.60.

3.2 Convergence and stability of hybrid LBM applied to the heterogeneous tissue problem

Henceforth employing the hybrid LBM scheme and focusing on the heterogeneous tissue model depicted in Figure 1(b), the effect of the membrane permeability on the truncation error is demonstrated in Figure 6. The results are obtained for a circular fiber and a square domain with $D_{in} = 2\ \mu m^2/ms$ and $D_{ex} = 3\ \mu m^2/ms$. The spatial convergence is second order for all values of the permeability.

Given that the first term in the factor $\exp[-j\ \gamma[\boldsymbol{x} \cdot \boldsymbol{G}(t)]\ \delta t' - (T_2)^{-1}\delta t']$ in Equation (4) changes only the phase of $\boldsymbol{M}$ while the second term decays in time, the numerical stability of the hybrid LBM scheme is controlled by the stability of the classical LBM applied for Equation (5). LBM is unconditionally stable for the diffusion equation [50]. This conclusion does not cover the effect of the membrane boundary condition on numerical stability of the numerical scheme. In order to provide stability bounds in that case, we rely on the results of [42] and specifically, their Equations (34b) and (35b) and a numerical example in their section 3.1.1. Given our Equation (B.5), the lower stability bound is $c_{d1} = -1.6$, while the lowest value we obtain for $\Delta = 0.5$ is $c_{d1} = 2(\Delta - 1) = -1$, so the LBM scheme with membrane boundary conditions is always stable. For variable Δ, the lowest possible value is obtained for $\Delta = 0$ and is $c_{d1} = -2$, which for $\tau < 0.6$, produces an unstable scheme. Hence, for membrane boundaries not located halfway between lattice nodes, there is a restriction on τ in order to maintain numerical stability.
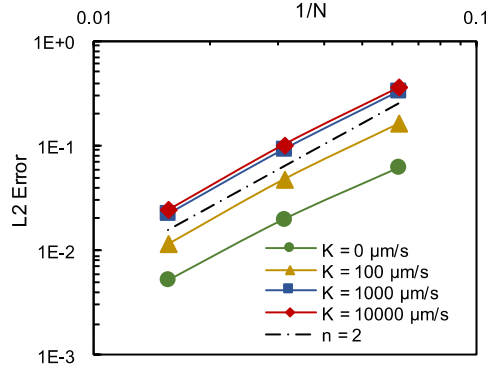
Figure 6. Effect of membrane permeability on spatial convergence of the hybrid LBM scheme for the heterogeneous periodic tissue model, with $\tau = 0.62$ and pulse parameters b = 1000 s/mm^2, $\delta = 4$ ms, $\Delta T = 10$ ms and TE = 20 ms.
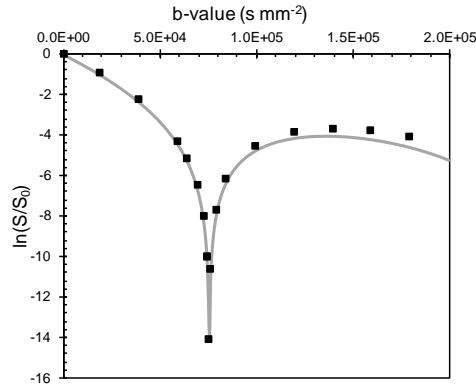

Figure 7. Plot of $-b\,(ADC)$ vs b-value (s/mm^2) for restricted diffusion in a cylinder. The solid line corresponds to the analytical solution given by Equation (32). The computed solution (solid squares) begins to diverge at higher b-values due to error from increased gradient strength.

3.3 Effect of MR parameters on apparent diffusion coefficient (ADC)

The hybrid LBM scheme predictions are compared with the analytical solution for cylinders of radius R surrounded by an impermeable membrane at the limit of infinite separation between the gradient pulses and infinitely short gradient duration (cf. Figure 2; $\Delta T \rightarrow \infty, \ \delta \rightarrow 0$). The analytical solution is given by [54]

$$\frac{S}{S_0} = \frac{[2\,J_1(\gamma|\boldsymbol{G}_0|\,\delta\,R)]^2}{(\gamma|\boldsymbol{G}_0|\,\delta\,R)^2} \tag{32}$$

The domain used for this simulation was defined by a cylinder of radius $R = 4.4\ \mu m$ with $D_{in} = 2\ \mu m^2 ms^{-1}, T_2 = 110$ ms, which is delineated by an impermeable boundary. This is a good approximation for the analytical solution given above, which assumes $D_{in}\,\Delta T \gg R^2$. A PGSE pulse was used with timing parameters TE = 200 ms, $\Delta T = 100$ ms and $\delta = 0.3$ ms. The simulations were performed with $\delta t = 0.01$ ms, $\delta x = 0.4\ \mu m$ and $\tau < 0.6$. The LBM predictions compare well with the analytical solution in Figure 7. Differences appear only at higher b-values that are not of practical interest.
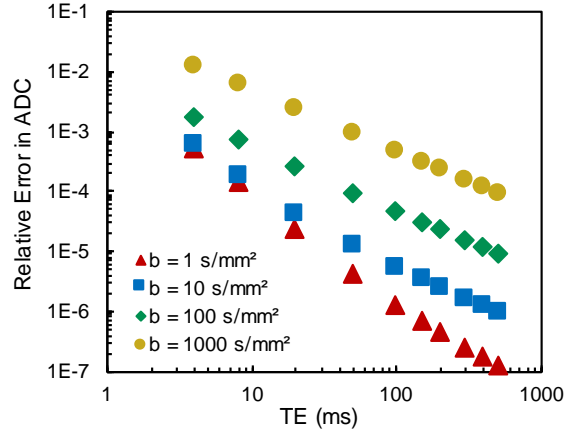
Figure 8. Relative error in ADC vs. TE for a homogenous domain using different b-values with timing parameters $\delta = \Delta T = TE/2$.

The effect of pulse timing parameters was also investigated. A PGSE pulse was utilized with TE ranging from 4 to 500 ms. A 2-D homogeneous REV of 80 μm × 80 μm was used with $\delta t = 0.01$ ms, $\delta x = 0.4\ \mu m$, and $\tau = 0.875$. Four different b-values of 1, 10, 100, and 1000 s mm^{-2} were used, while $\delta = \Delta T = TE/2$. Results of the relative error in the extracted ADC compared with the theoretical diffusion coefficient and presented in Figure 8. It can be seen that the error decreases as TE increases, and this decrease becomes faster as b decreases. This is consistent with the expectation that the Bloch-Torrey equation is approximated by the diffusion equation as TE (and the delay ΔT between the gradient pulses) increases. As Equation (2) implies, $b \sim |G_0|^2\ TE^3$, which indicates that for fixed b-value, $|G_0|^2 \sim b\ TE^{-3}$, i.e., the size reaction term R in the right hand side of (A2) decreases as TE increases. The above order of magnitude analysis also explains the effect of the b-value observed in Figure 8.

Convergence of the model was also checked against the analytical solution for a square array of circular cylinders with infinite permeability. The leading order term of the analytical form of the effective (apparent) diffusion coefficient for conducting cylinders was derived in [55]:

$$D = D_{ex}\left[1 - \frac{2f}{T + f - \dfrac{0.305827 f^4 T}{T^2 - 1.402958 f^8} - \dfrac{0.013362 f^8}{T}}\right] + h.o.t. \qquad (33)$$

where $T = (1 + D_{in}/D_{ex})/(1 - D_{in}/D_{ex})$ and f is the packing fraction of the cylinders. The equation given above is only accurate for certain values of T and f. For our purposes, comparisons will be made of D with $ADC\ (\Delta T \to \infty)$ for $T < 2$ and $f \le 0.52$, where the analytical solution is accurate to four decimal places.

First, a square arrangement of 60 μm diameter cylinders in a periodic 80 μm × 80 μm domain was employed. The diffusion coefficients were $D_{in} = 1.5\ \mu m^2/ms$ and $D_{ex} = 2\ \mu m^2/ms$. The above geometrical and diffusion parameters are representative of muscle fiber arrangements. The steps δx and δt were adjusted such that $\tau = 0.875$ inside and $\tau = 0.78125$ outside the cylinders. Simulations were performed for TE = 100 and 200 ms and b values of 1, 500 and 1000 s mm^{-2}. Results for these simulations are shown in Figure 9, where it can be seen again that the convergence of the numerical solution to the analytical result is dependent on both TE and b values. For a given set of TE and b, the solution converges to a value that is offset by some amount from the analytical solution (33) as δx decreases. Larger TE values decrease the error because this

15

means longer ΔT values ($\Delta T = TE/2$). The analytical solution D should approach ADC as $\Delta T \to \infty$, so the offset value decreases as ΔT increases. It is worth noting that, as with the homogenous domain case, simulations with smaller b values reach the offset value faster as δx decreases, than those with large b values. Larger b values correspond to larger gradients, leading to higher spatial resolution requirements to fully resolve these gradients.
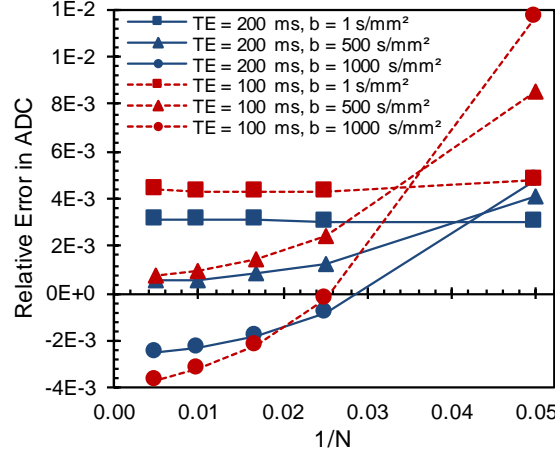

Figure 9. Relative error in computed ADC vs. 1/N (δx/L) for a square periodic array of cylinders with differing intra- and extra-cellular diffusion coefficients. Positive values indicate that ADC is larger than the analytical solution.
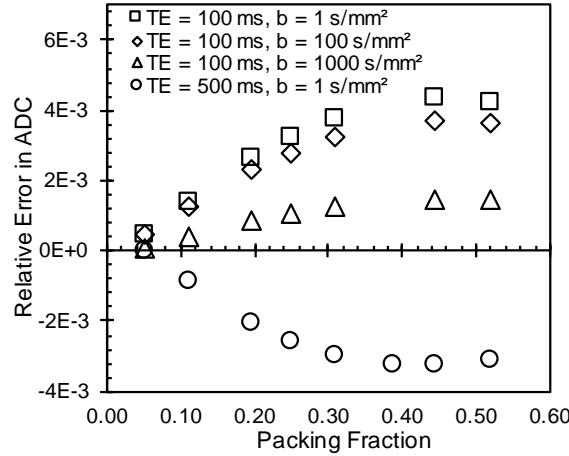

Figure 10. Relative error in computed ADC vs. packing fraction for a square periodic array.

Second, simulations were performed with the domain size held constant while the cylinder diameter was varied. Figure 10 shows results for multiple packing fractions and for TE = 100 ms with b = 1, 100, 1000 s mm^{-2} and TE = 500 ms with b = 1 s mm^{-2}. For the same TE, the error increases (in absolute value) as the packing fraction increases. As the packing fraction decreases, the cylinder diameter decreases and the solution approaches that for a homogeneous domain (consisting of only the external compartment), which exhibits less spatial property variation and therefore lower spatial error.
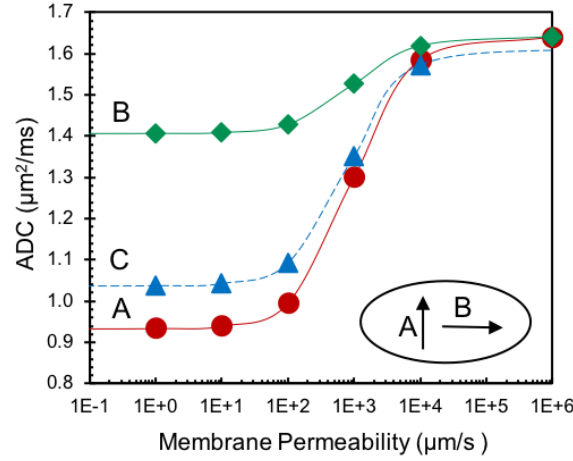
Figure 11. Effect of myocyte cross-section ellipticity and membrane permeability on computed ADC. Case A and B correspond to diffusion gradients applied perpendicular and parallel to the major axis of the elliptical cross-section, respectively. The insert depicts the gradient directions relative to the cross-section. Case C corresponds to myocytes with circular cross-section.

3.4 Effect of membrane permeability on ADC asymmetry

Seeking to explain the well-documented DTI signal asymmetry on planes perpendicular to the local muscle fiber direction, Karampinos et al. [6] proposed a tissue model that abstracts the myocytes as cylinders of infinite length with an elliptical cross section, and extended the analytical two-compartment white matter model of [56] to model the dMRI signal in muscle. We are focusing here on the continuum version of that tissue model, which allows the direct study of the effect of membrane permeability, rather than indirectly through the definition of mean residence times of spins in the two compartments. A square arrangement of elliptical cylinders in an $80\ \mu m \times 80\ \mu m$ REV was considered, and all simulations were performed for five membrane permeability values: K = 1, 10, 100, 1000, 10000, and 100,000 μm s-^{1}, and with δt =0.01 ms, $\delta x = 0.4\ \mu m$. The cylinder cross-sections are ellipses with a major-axis diameter of 76 μm and a major/minor axis ratio of 0.7. A PGSE sequence was used with TE = 56 ms, ΔT = 40 ms and δ = 16 ms. The physical parameters were $D_{in} = 1.5\ \mu m^2/ms\ D_{ex} = 2\ \mu m^2/ms$, and $T_2 = 110\ ms$ (same inside and outside the cylinder). Simulations were performed with the gradient aligned perpendicular to the major axis (Case A) and parallel to the major axis (Case B) of the ellipse. Additionally, a simulation for circular cylinders with a diameter 63.56 μm and the same packing fraction as Cases A and B was performed (Case C).

Simulations were performed over a range of b values and a linear curve fit was used to determine the ADC based on Equation (3). Figure 11 gives a plot of ADC as a function of the permeability for the three cases. We note a wider range of ADC values for the gradient applied perpendicular to the major axis (Case A) than when the gradient is applied parallel to the major axis (Case B). This difference is large for small K values and becomes negligible as K becomes sufficiently large. Since diffusion is only measured in the direction of the gradient, Case A introduces a larger barrier to diffusion than Case B and so the lower ADC measured for Case A when permeability is low is consistent with expectations. For low permeability values, Case C is between Cases A and B. The cross-section presented to the gradient direction in Case C is between the cross-sections presented by Cases A and B, suggesting that at low permeabilities this cross section is a determining factor in ADC. However, as permeability increases, all three cases appear

17

to converge upon a single value. Additional simulation results (nor presented here) indicate that the general monotonic s-shape of the ADC vs. K curve shown in Figure 11 is maintained for other cylinder cross-sections and combinations of D_{in}, D_{ex} and T_2 (different inside and outside the cylinder) parameters. Specifically for circular cylinders (like Case C), the ADC varies significantly only in the range 100 µm s⁻¹<K< 10,000 µm s⁻¹, as per Figure 11. Outside this range, the ADC value reaches either the impermeable limit or the infinite permeability limit.
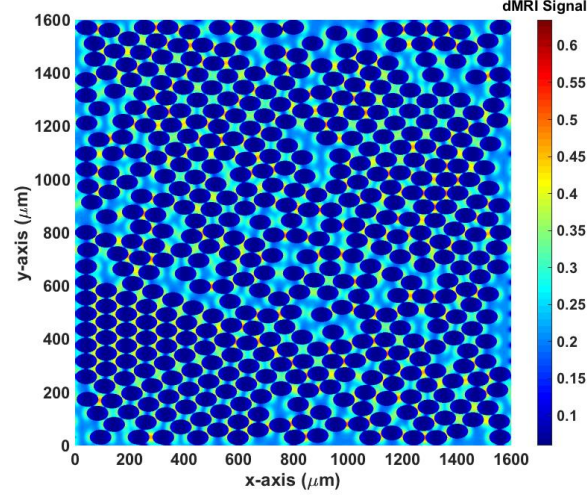

Figure 12. Field map of magnetization signal for random array of myocytes with elliptical cross-section at t= TE and diffusion gradient applied along x. The major axis of the cylindrical cross section is 80 μm, the ratio of minor to major axis is 0.7, the packing fraction is 0.6398, and the membrane permeability is K= 1 µm/s. Diffusion coefficients are $D_{in} = 1.9 \ \mu m^2/ms$ and $D_{ex} = 2.0 \ \mu m^2/ms$ while relaxation times are $T_{2,in} = 32 \ ms$ and $T_{2,ex} = 125 \ ms$.

3.5 Simulation in 2-D REV with disordered array of cylinders: effect of averaging domain size

Building on the results of the previous subsection, we pursue the simulation of the dMRI signal in a more realistic assemblage of myocytes, which is represented here by a disordered array of cylinders of identical elliptical cross-sections. First, a cylinder packing method was developed. This method begins with a sparsely packed periodic array of elliptical cylinders, with aligned major and minor axes, and then proceeds to translate each cylinder in small random steps in 2D until its perimeter crosses a neighboring cylinder. Performing this sequentially for all cylinders transforms the originally periodic array to a disordered one, while maintaining the alignment of major/minor axes of the ellipses. This procedure is performed many times, and additional cylinders added anytime there is adequate space in the boundaries of the REV. Cylinders are added in the REV so that the packing fraction increases. The initial sparseness allows us to avoid the cylinders getting "jammed" and thus reach a dense packing, as shown in Figure 12. However, the packing method employed does not prevent the formation of (crystalline) regions with short-range order. This is caused by the alignment of the elliptical cross sections; they are identical and all have their major axis parallel to the x-axis. Local crystallization is unavoidable for high packing fractions, but needs to be addressed in the context of more (physiologically) realistic myocyte cross-sections, which is outside the scope of the present investigation.

Second, we address the question of how large the REV involving disordered array should be so that volume-average properties, like the ADC, do not depend on the boundary conditions, which are periodic in space. The expectation is that as the averaging regime becomes larger, the effect of

the boundary on ADC will diminish. The simulation involves an REV of 1600 μm × 1600 μm, with δt =0.04 ms, $\delta x = 1.6\ \mu m$. The hybrid LBM scheme was performed for a PGSE pulse with diffusion gradient with b= 572 s/mm^2 applied along the coordinate x, and timing parameters TE = 56 ms, ΔT=40 ms and δ=16 ms. The field map of the magnetization at t = TE is shown in Figure 12. The geometrical and physical properties of the cells are given in the figure caption. The ADC was calculated by averaging the signal over square regimes of decreasing size and centered in REV. The results shown in Table 1 indicate ADC varies by less than 1% as the regime is reduced to 1/3 of the original size. This means that a good approximation of the ADC can be obtained by averaging over a regime corresponding to a disordered array of approximately 5 × 5 cylinders. This is in agreement with prior predictions of the size of the developing regime in problems involving advection-reaction in domains with cylinder arrays [57].

Table 1. Calculated ADC by averaging signal over square regimes of decreasing size and centered in 2D REV (as fractions of REV size).

REV centered fraction	ADC (μm^2/ms)
1/3	1.4111
1/2	1.4085
2/3	1.4011
1	1.4116

3.6 Three dimensional version of hybrid LBM scheme

All previous results thus far have been confined to 2D using a D2Q5 stencil, however, the extension of the hybrid LBM scheme to 3D is straightforward. To demonstrate, a D3Q7 stencil (Figure 3) was used to simulate the dMRI signal by solving Equation (1) in 3D in a period array of permeable cylinders of circular cross section, whose axis is aligned with the z coordinate (Figure 1(a)). The cylinder diameter is 55 μm and the packing fraction is 0.65, while the physical parameters are $D_{in} = 1.5\ \mu m^2/ms$, $D_{ex} = 2\ \mu m^2/ms$, $T_{2,in} = 30\ ms$, $T_{2,ex} = 10\ ms$ and K = 10 μm/s. The REV is a rectangular prism with grid size 55 × 55 × 5, and the temporal and spatial steps are δt =0.025 ms, and $\delta x = 1.0\ \mu m$. Modified periodic boundary conditions (section 2.3.1) were implemented on all external boundaries, and a PGSE sequence with b = 1000 s/mm^2, TE = 24 ms, ΔT = 20 ms, and δ = 4 ms was used. The gradient $\boldsymbol{G}_0$ was applied along an oblique direction with directional cosines $\left(\frac{1}{\sqrt{3}}, \frac{1}{\sqrt{3}}, \frac{1}{\sqrt{3}}\right)$. The field map of the magnetization at t= TE is shown in Figure 13. Because the cylinder axis is aligned with the z-direction and the boundary conditions are periodic, there is no z-dependence in the signal, even though the gradient $\boldsymbol{G}_0$ has a nonzero z-component. This spatial symmetry of the result is a consequence of the symmetry of the inner boundaries and outer boundary conditions, and does not constitute a limitation of the general 3D implementation of the LBM scheme. As Figure 13 indicates, the field map is the same on all z-slices. This symmetry is exploited in the next section in order to keep using the 3D version of the code.
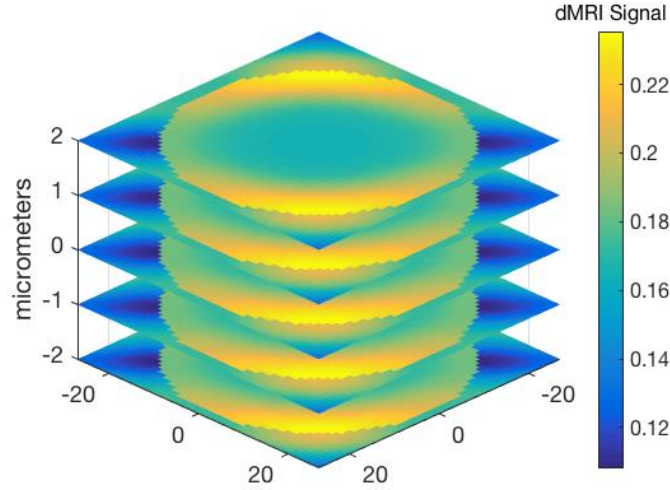
Figure 13. Field map of 3D magnetization on a cross-section at each grid point in the z-direction (exploded view). Due to the cylinder alignment and periodic boundary conditions there is no z-dependence in the signal, even though the gradient was applied obliquely.

3.7 Parallelization of LBM hybrid scheme

Considering the diameter of skeletal muscle fiber ($\sim$ 80 μm) relative to the typical size of a dMRI voxel ($\sim 1mm^3$), the simulation of the magnetization field in a voxel would result in a very large computational problem (10^{3d} nodes for d dimensions). This spatial resolution is required on the basis of the results obtained so far. Although the structural hierarchy of the muscle can be exploited to reduce the size of this problem somewhat, it is still necessary to develop an efficient code adapted to LBM to solve this problem directly. We investigate a parallel implementation of the hybrid LBM scheme based on domain decomposition [58] and a Fortran code with message passage interface (MPI). This implementation starts by partitioning the REV into multiple non-overlapping domains. Each domain is assigned to a separate MPI process so it can run in parallel with the other domains. We employ the 3D version of the LBM code (D3Q7 stencil) on an REV that is a thin rectangular prism with grid size $N \times N \times 1$. For the domain decomposition, the REV is partitioned into multiple strips and each strip is handled by one MPI process, which in turn is assigned to one core. For every time step, each core executes the hybrid LBM algorithm over the assigned domain and exchanges boundary information with adjacent strips while the two strips at the edges of the REV exchange boundary information with each other subject to the modified periodic boundary conditions in 3D. Two quantities must be minimized in order to maximize the parallelization efficiency: the number of neighboring domains each individual process must communicate with and the amount of information passed between each domain. Here we focused on minimizing the number of neighboring domains with which each individual MPI process communicates, while holding the length of the boundary between strips fixed. The performance of the parallel implementation is quantified in terms of the following ratios (p denotes the number of cores)

$$\text{Speedup} = \frac{\text{Execution time with 2 cores}}{\text{Execution time with } p \text{ cores}} \quad ; \qquad \text{Parallel efficiency} = \frac{\text{Speedup}}{p} \qquad (34)$$
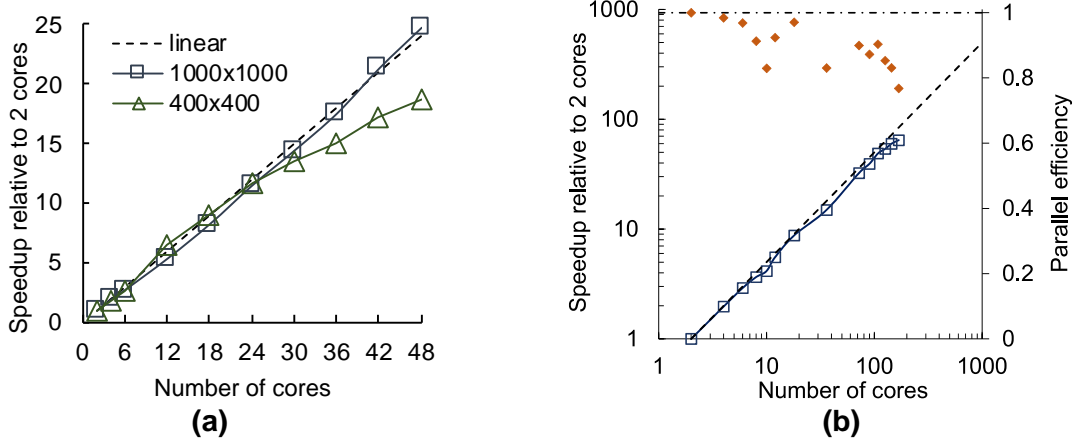
20

Figure 14. Performance of hybrid LBM code after domain decomposition and parallelization with one-to-one mapping between domains, MPI processes and computer cores. **(a)** Speedup for N=400 and N=1000 with 2 to 48 cores. **(b)** Speedup (open symbols) and parallel efficiency (solid symbols) for N=1000 with 2 to 168 cores.

In order to investigate speedup due to parallelization, a parallel code was developed using Fortran 90 with Intel's IFORT v14.0.2 compiler and MVAPICH2 v2.1. Simulations were run on XSEDE's Comet cluster [59] which consists of 1944 nodes with 2 x 12 core CPU processors (Intel Xeon E5-2680 v3 2.5 Ghz), and 128 GB DDR4 DRAM running CentOS 6.7. Two homogenous REVs with square x, y cross-sections with side lengths of 0.4 mm and 1.0 mm were simulated with TE = 24 ms, τ =0.58, δt =0.010 ms, and $\delta x = 1.0\ \mu m$. These domains correspond to $N \times N \times 1$ grids with sizes $N = 400$ and $N = 1000$, respectively. Other domain and timing parameters were D = 2 μm^2/ms, T_2 = 100 ms, b = 1179 s/mm^2 (q = 40/mm^2), TE = 24 ms, ΔT = 20 ms, and δ = 4 ms. LBM algorithms require high memory throughput and, as such, are often limited by memory bandwidth [60]. To examine the scaling of the algorithm beyond this known limitation, scaling simulations were preformed first by using up to 48 cores and adjusting the number of cores per node so the entire problem could be held in cache when possible. Due to the current of the MPI implementation, it is not possible to run the code with only one core, hence the definition of speedup ratios in Equation (34). All simulations were repeated 5 times and the average execution time was used to determine how the code execution time scales with the number of cores. The results are shown in Figure 14(a), and indicate that for $N = 1000$ the speedup is linear over the whole range. For $N = 400$, there is linear speedup up to 24 cores, before the performance begins to degrade due to MPI overhead costs. This occurs for the smaller domain because the cost of message passing between cores scales as $\sim N$ while the number of operations per core scales as $\sim N^2/p$, for the current partitioning of the REV. (p denotes number of cores.) So the cost of message passing relative to operation count per core scales as $\sim p/N$, which implies that performance degrades at a lower number of cores for coarser grids. Code profiling of both grids on two cores revealed that execution time was approximately equally split between the streaming (~24%) and collision (~23%) steps while computing the equilibrium distribution accounted for ~17% of the code execution time and the hybrid step of computing precession and relaxation accounted for ~10% of the execution time. The average execution time for two cores was 376.8 seconds for $N = 1000$ and 46.7 seconds for $N = 400$. Simulations were also performed for N = 1000 using up to 168 cores, and the results plotted in Figure 14(b) indicate that the code exhibits ideal (linear) speedup, while reaching a minimum parallel efficiency of 77%.

4. Discussion

Reporting on the first implementation of LBM to solve the Bloch-Torrey equation (1), we proposed the hybrid LBM scheme summarized by Equation (17). The fundamental difference with the classical version of LBM, which is given by replacing Equation (12) by Equation (A12), is the factorization of the operator (4), which splits the reaction and diffusion temporal discretization. This splitting addresses the stiffness of the problem, which is characterized by the disparity between reaction and diffusion time scales, as discussed in the first paragraph of Appendix A. Based on comparisons with limiting cases (when analytical solutions are available), we demonstrated that the hybrid scheme is more accurate than the classical LBM scheme. Both schemes are second order-accurate in space and first-order in time. Since τ and D are kept constant, Equation (8) implies that $\delta t \sim \delta x^2$. In other words, we need to decrease δt while maintaining $\delta t / \delta x^2$ constant in order to increase the approximation accuracy. As Equation (A15) indicates, the time step limitation for the classical LBM is more restrictive than that for the hybrid LBM, which is given by (A10). This implies that the accurate integration of (A1) with classical LBM requires a four orders of magnitude smaller time step than with the hybrid scheme for $L \sim 100 \ \mu m$, with the concomitant requirement that the grid size has to decrease by eight orders of magnitude ($\delta x^2 \sim \delta t$). This result explains why the truncation error of the classical scheme is higher for the larger domain size, cf. Figure 5.

      Like the classical LBM scheme, the hybrid version based on the time splitting scheme described by Equations (4) and (6) is unconditionally stable (because both time splits are stable), so the step sizes are determined by approximation accuracy considerations. Concerning the choice of δt and $\delta t'$, and in view of (A10), let us consider the limitations placed on the diffusion time step δt for realistic values of the diffusion coefficients in tissue. For typical values $\tau \sim 0.6$ and $D \sim 2 \frac{\mu m^2}{ms}$, Equation (8) requires $\frac{\delta t}{\delta x^2} \sim 0.02 \ \frac{ms^2}{\mu m}$. For a spatial resolution of $\delta x \sim 1 \ \mu m$ in an REV with $L \sim 100 \ \mu m$, this requires $\delta t \sim 0.02 \ ms$. Given that this diffusion step also satisfies the requirement for the reaction step in (A10), we have employed $\delta t = \delta t'$ in the present study. It is also worth providing formal estimates of the truncation errors in this case. The spatial error is $O\left(\frac{\delta x^2}{L^2}\right) \sim 10^{-4}$ and the temporal error is $O\left(\frac{\delta t}{TE}\right) \sim 10^{-4}$ for $TE \sim 100 \ ms$. Formal optimization of the hybrid LBM would involve a study of the variation of the truncation error as a function of τ, like in [61, 62], and an investigation of varying the sequence or the step size ($\delta t \neq \delta t'$) of the diffusion and reaction splits [48], but both are outside the scope of the present study. Improved explicit [34, 37] and implicit [35, 36] temporal integration schemes have been proposed for the solution of the Bloch-Torrey equation with the finite element method. Especially relevant to the present work based on the hybrid LBM, the first-order stabilized explicit Runge-Kutta scheme (called Runge-Kutta-Chebyshev scheme) was used in an adaptive temporal integration code employed by Li et al. [37] to reduce the simulation time. Whereas the number of time steps for LBM is approximately $N_t = \frac{TE}{\delta t} \sim \frac{TE}{\delta x^2} \frac{D}{\delta x^2}$, the Runge-Kutta-Chebyshev scheme requires $\sim \frac{TE}{s} \frac{D}{\delta x^2}$ steps on average (since the time step is variable), where s is the number of stages. The advantage of the latter is evident during the times when the dMRI gradient is turned off and the spatial discretization is relatively coarse [37]. It is worth mentioning in passing that in the Crank-Nicolson finite element scheme [36], which is second-order in time, the time step size needed to be quite small at high membrane permeabilities, reaching the range employed in the hybrid LBM scheme. The disadvantage of LBM schemes relative to higher order temporal schemes is offset by the amenability of the former to parallelization. Parallel computing is where LBM schemes have a performance advantage over

finite difference or finite element schemes. Our LBM code for solving the Bloch-Torrey equation on a $1000 \times 1000 \times 1$ grid exhibits a parallel efficiency of 77% at 168 cores, vs. an efficiency of ~55% for the finite element scheme with ~3.5 million degrees of freedom at 256 cores [36]. Our speedup is optimal (linear) for the whole range, cf. Figure 14. Our parallelization algorithm relies on an uncomplicated domain decomposition scheme and one-to-one mapping of the MPI processes to CPU cores. Further gains in performance are anticipated by accounting for special computer architecture or by employing GPU cores [44, 46].

      The hybrid LBM method shares the clear advantage of LBM methods in terms of using uniform grids to discretize curved boundaries between various compartments in the REV, while retaining second-order spatial accuracy and stability. Consistent with the kinetic nature of the LBM scheme, the membrane boundary conditions (29) connect the particle distribution functions at either side the interface directly with the membrane permeability K (defined in Equation (28)), and avoid the need to approximate transmembrane derivatives, as is the case with finite difference or finite element schemes. Locating the curved cylindrical boundaries exactly half-way between lattice nodes ($\Delta = 0.5$) can decrease the formal spatial accuracy [51]. Nevertheless, the accuracy of the volumetric average over the REV (which expresses the signal in dMRI) does not seem to be affected by this simplification, cf. Figures 6-7. If the need arises to accommodate large boundary gradients, alternate schemes with $\Delta \neq 0.5$ values can be incorporated, with a small penalty of involving extra interfacial lattice nodes, cf. Appendix B. The extension from 2D (D2Q5 stencil) to 3D (D3Q7 stencil) is straightforward owing to the simplicity of the spatial discretization and implementation of the boundary conditions. In terms of memory allocation, the LBM scheme requires a total allocation of $44 \times N^3$ for the numerical integration of the Bloch-Torrey equation for $N \times N \times N$ lattices (in 3D). Based on these estimates we can describe the complexity of the hybrid LBM scheme by $44 \times N_t \times N^3$, which is $\sim 10^{10}$, given the discretization parameters discussed in the previous paragraph for $\sim 10^{-4}$ truncation error. Analysis of the computing performance of Monte Carlo methods to integrate the Bloch-Torrey equation in two-compartment tissue models morphologically similar to the ones used in this study indicates that a minimum complexity of $\sim 10^9$ is needed in order to avoid statistical error [28, 38]. Moreover, Yeh et al. [28] repeat each simulation 10 times, thus raising this minimum to $\sim 10^{10}$. Consideration of the effect of thin cell membranes on the computing performance increases the complexity significantly. A comparison between LBM and Monte Carlo indicates that the former performs better when (interfacial) surface effects are important. Finally, the imposition of the external periodic conditions is straightforward for the hybrid LBM, in contrast with the finite element scheme [36] where they had to be approximated by introducing an artificial permeability to mimic diffusion at the external boundaries.

      We conclude with several comments regarding possible extensions of the hybrid LBM scheme developed here. Although the LBM scheme was applied to the simulation of dMRI signal from muscle tissue using a specific MRI sequence, the formulation is very general and it can accommodate other transport phenomena, multiple tissue compartments, and MRI sequences. The scheme can be readily extended to incorporate more complex physics and be applied in the study of other tissue models (e.g. axons with myelin sheaths embedded in glial matrix). It can also accommodate more complex dMRI gradient waveforms and sequences involving other MRI contrast mechanisms (e.g. perfusion, magnetic susceptibility, elastography, etc.), or imaging gradients (slice selection, phase encoding, or readout). Starting with its first application for modeling unrestricted diffusion [63], LBM has since accommodated anisotropic diffusion and advection [64, 65], coupled diffusion [50] and coupled reaction-diffusion between multiple species [48, 62], finite cell membrane permeability [66], phase field models [67], and interstitial flow [68-

70]. Such processes are pertinent to biophysics problems involving transport and evolution of large biomolecules in blood-perfused cellular systems, and physics other than diffusion. For example, LBM was applied to model protein diffusion inside mammalian cells [71] and to model cardiac electrophysiology [46]. As an additional indication of its versatility, LBM has been recently employed to integrate fractional order diffusion-advection-reaction equations [72]. This is not to say that other numerical methods could not have been employed for the phenomena mentioned above, but rather, owing to the local nature of the operations, the same LBM formulation can be easily adapted to simulate accurately and efficiently a vast range of physical phenomena.

5. Conclusions

Motivated by the need to interpret the dMRI signal from skeletal muscle tissue, we have laid the foundation and performed the analysis of a hybrid implementation of the LBM to integrate the Bloch-Torrey equation in heterogeneous tissue models. A bi-phasic tissue model is considered consisting of cylindrical inclusions (representing myocytes) delineated by thin permeable membranes (sarcolemma) and surrounded by a matrix (endomysium). In its current implementation, the hybrid LBM scheme accommodates finite sarcolemma permeability, piece-wise uniform diffusion coefficients and a wide range of dMRI parameters, outer periodic boundary conditions, and interphase conditions accounting for flux continuity. By splitting the reaction and diffusion time steps, the algorithm maintains the explicit nature of the (classical) LBM implementation. We have shown via truncation error analysis and numerical tests that this splitting obviates the requirement of small temporal steps introduced by the strong reaction term in the Bloch-Torrey equation. Another attractive feature of the classical LBM scheme is also maintained here: the phase boundaries are discretized in uniform 2D and 3D lattices by locating the curved cylindrical boundaries halfway between lattice nodes. We have shown that the hybrid scheme retains the second-order spatial accuracy and stability within a wide range of membrane permeability values and typical dMRI parameter values. This allows the study of the dMRI signal in large disordered arrays of cylinders representing more complex inner boundaries. Finally, our results indicate that the associated LBM code is very compact and can be easily parallelized and executed efficiently on a general multi-core computer. Currently, the parallel algorithm is based on a straightforward spatial domain decomposition scheme, and does not involve any modification of the message passing between cores or an attempt to exploit the architecture of the particular computer system used. The speedup of 3D parallel code for N = 1000 is optimal for up to 168 CPU cores and maintains a parallel efficiency above 77%.

APPENDIX A

The first part of this appendix presents a truncation error analysis of the splitting scheme implemented in the hybrid LBM. There are two methods to derive the macroscopic equation from the evolution of the particle probability distribution function: multiple time scales (Chapman-Enskog expansion), and asymptotic analysis [61, 65]; here we employ a combination of them. First, we present a scaling analysis of the Bloch-Torrey differential equation (1), rewritten for a general gradient pulse $G(t) = G_0 f(t)$ and for piece-wise uniform diffusion coefficients as follows

$$\frac{\partial M}{\partial t} = -j\,\gamma[x \cdot G_0\, f(t)]M \quad -\frac{M}{T_2} \quad + D\nabla \cdot \nabla M \qquad (A1)$$

$$\gamma L|G_0| \sim \frac{1}{ms} \qquad \frac{1}{T_2} \sim \frac{10^{-2}}{ms} \qquad \frac{D}{L^2} \sim \frac{10^{-4}}{ms}$$

The above equation is a homogeneous reaction-diffusion differential equation so the relative order of magnitude of the various terms does not depend on the magnitude of M. Eq. (A1) is defined in $t \in [0, TE]$ and $x \in$ REV. Using the REV size L as a length scale (on the order of the diameter of a myocyte $\sim 100\ \mu m$), typical whole-body MRI scanner parameters, and physical properties for muscle [6], an order of magnitude analysis of the terms in the right hand side of (A1) reveals the disparity between the reaction (first and second term) and diffusion (third term) time scales. The reaction rates are more than two orders of magnitude faster than the diffusion rate. This is the motivation for the splitting scheme associated with the hybrid LBM, which is a concept that has been explored in prior studies of such models [48].

Second, we can rename the linear reaction operator in (A1) as follows

$$\frac{\partial M}{\partial t} = R(x, t)\,M + D\nabla \cdot \nabla M\,, \quad \text{with} \quad R(x, t) = -j\,\gamma[x \cdot G_0\, f(t)] - \frac{1}{T_2} \qquad (A2)$$

and generalize Eq. (4) to express the evolution of magnetization starting past a reference time instant $t^k \in [0, t_E]$

$$M(x, t) = \exp\left[\int_{t^k}^{t} R(x, t'')\, dt''\right] M'(x, t) \quad \text{for} \quad t \geq t^k \qquad (A3)$$

Note that $M(x, t^k) = M'(x, t^k)$. Differentiate (A3) with respect to time to obtain

$$\frac{\partial}{\partial t} M(x, t) = R(x, t)M(x, t) + E(x, t^k; \delta t')\frac{\partial}{\partial t} M'(x, t) \qquad (A4)$$

where

$$E(x, t^k; \delta t') = \exp\left[\int_{t^k}^{t^k + \delta t'} R(x, t'')\, dt''\right], \quad \text{and } \delta t' \geq 0 \qquad (A5)$$

Let us suppress all dependent variables everywhere except in the expression $E(x, t^k; \delta t')$, and require that M' obeys the diffusion equation, within a certain truncation error TE_D

$$\frac{\partial}{\partial t} M' = D\nabla \cdot \nabla M' + TE_D \qquad (A6)$$

so (A4) becomes

$$\frac{\partial}{\partial t} \boldsymbol{M} = \boldsymbol{R} \ \boldsymbol{M} + \ \boldsymbol{E}(\boldsymbol{x}, t^k; \delta t') \ [D\nabla \cdot \nabla \boldsymbol{M}' + TE_D] \tag{A7}$$

Using (A3), we can show that

$$\boldsymbol{E}(\boldsymbol{x}, t^k; \delta t') \ \nabla \cdot \nabla \boldsymbol{M}' = \ \nabla \cdot \nabla \boldsymbol{M} + 2j\gamma F(t^k; \delta t') \ \boldsymbol{G}_0 \cdot \nabla \boldsymbol{M} - \gamma^2 F^2(t^k; \delta t') \ |\boldsymbol{G}_0|^2 \ \boldsymbol{M}$$

where

$$F(t^k; \delta t') = \int_{t^k}^{t^k + \delta t'} f(t'')dt'' \tag{A8}$$

This allows casting (A7) in the form of (A2)

$$\frac{\partial}{\partial t} \boldsymbol{M} = \boldsymbol{R} \ \boldsymbol{M} + \ D\nabla \cdot \nabla \boldsymbol{M} + [2j\gamma D \ F(t^k; \delta t') \ \boldsymbol{G}_0 \cdot \nabla \boldsymbol{M} - \gamma^2 D \ F^2(t^k; \delta t') \ |\boldsymbol{G}_0|^2 \boldsymbol{M}]$$
$$+ [\boldsymbol{E}(\boldsymbol{x}, t^k; \delta t') \ TE_D] \tag{A9}$$

The terms contained in the two square brackets constitute the truncation error of the hybrid LBM scheme proposed here. The terms in the first bracket containing the expression (A8) correspond to the error introduced in the treatment of the reaction part of (A2) according to (A3), and their magnitude can be estimated by assessing the magnitude of the integral in (A8). By recognizing that $f(t) \sim O(1)$, we can easily see that $F(t^k; \delta t') \sim O(\delta t')$, so that the formal order of magnitude of the two reaction truncation error terms is $\gamma D |\boldsymbol{G}_0| \frac{1}{L} \delta t'$ and $\gamma^2 D |\boldsymbol{G}_0|^2 \delta t'^2$. In order for (A9) to be consistent with (A2), both these terms have to be much smaller than the smallest term in (A2), which is the diffusion term according to the order of magnitude analysis of (A1). Since the relative order of the diffusion term is $\frac{D}{L^2}$, this requirement implies $\gamma L |\boldsymbol{G}_0| \ \delta t' \ll 1$ and $(\gamma L |\boldsymbol{G}_0| \ \delta t')^2 \ll 1$. The first requirement is more restrictive, so the formal constraint for the reaction time step becomes

$$\delta t' \ll \frac{1}{\gamma L |\boldsymbol{G}_0|} \sim ms \tag{A10}$$

Since the diffusion problem (A6) is integrated with the classical LBM scheme, we can estimate TE_D from a truncation error analysis of that scheme. This error can be obtained by modifying, according to our Equations (5) and (8), the expression (A23) obtained by the Chapman-Enskog expansion in the Appendix of [62], and by separating the effect of the diffusion time step δt from the lattice grid size δx

$$TE_D = 3 \ \delta t \ \frac{\tau^2 - \tau + \frac{1}{6}}{\tau - \frac{1}{2}} \frac{\partial^2 \boldsymbol{M}'}{\partial t^2} = \ \delta x^2 \ \left(\tau^2 - \tau + \frac{1}{6}\right) \frac{\partial^2 \boldsymbol{M}'}{\partial t^2} \tag{A11}$$

The expressions in (A11), which are equivalent since the ratio $\delta x^2 / \delta t$ is proportional to D, cf. Eq. (9), recover the known fact that the truncation error of the classical LBM is first order in time and second order in space. Returning to the last term in (A9), we can see that this is also the contribution of TE_D to the hybrid LBM error if we require that $\boldsymbol{E}(\boldsymbol{x}, t^k; \delta t') \sim O(1)$. Referring to Eqs (A2) and (A5), and recalling that $f(t) \sim O(1)$, this is accomplished by restricting the reaction time step $\delta t'$ so that $\gamma L |\boldsymbol{G}_0| \ \delta t' \ll 1$. This is the same requirement imposed in (A10), so the leading contribution to the overall truncation error of the diffusion term is $O(\delta t, \delta x^2)$, and of the reaction term is $O(\delta t')$.

The second part of this Appendix addresses the truncation error of the classical LBM applied in the solution of the Bloch-Torrey (A2), i.e. without the time splitting scheme (A3). This

involves a modification of the collision step of the LBM scheme described in Methods section, which unlike Eq. (12) now reads

$$\hat{g}_i(\pmb{x}, t) = g_i(\pmb{x}, t) - \frac{1}{\tau}\big[g_i(\pmb{x}, t) - g_i^{eq}(\pmb{x}, t)\big] + \delta t\, \omega_i\, \pmb{R}(\pmb{x}, t)\, \pmb{M}(\pmb{x}, t) \qquad \text{(A12)}$$

where $\pmb{M}(\pmb{x}, t)$ is computed by summing over g_i, as shown in Eq. (14). Including the reaction term in (A12), results in a different version of (A9):

$$\frac{\partial}{\partial t}\pmb{M} = \pmb{R}\,\pmb{M} + D\nabla \cdot \nabla \pmb{M} + TE_D + TE_R \qquad A(13)$$

The reaction truncation term, TE_R, can be evaluated by starting from the relevant truncation error expression (A23) in the Appendix of [62] (after correcting an error; the reaction term is only $O(\delta t)$ and not $O(\delta t^2)$).

$$TE_R = \tau\,\delta t\,\frac{\partial}{\partial t}[\pmb{R}\ \pmb{M}] = \tau\,\delta t\left[\frac{\partial \pmb{R}}{\partial t}\pmb{M} + \pmb{R}\frac{\partial \pmb{M}}{\partial t}\right]$$

and using (A2)

$$TE_R = \tau\,\delta t\left[\frac{\partial \pmb{R}}{\partial t}\pmb{M} + \pmb{R}(\pmb{R}\,\pmb{M} + D\nabla \cdot \nabla \pmb{M})\right] \qquad \text{(A14)}$$

Given the order of magnitude analysis performed for (A1), the leading order term in TE_R is the second term in (A14),

$$\tau\,\delta t\,\pmb{R}\,\pmb{R} \sim O\{\tau\,\delta t\,(\gamma L|\pmb{G}_0|)^2\}$$

Again for consistency, this truncation error term has to be much smaller than the smallest term in (A2), which is the diffusion term according to the order of magnitude analysis of (A1). Since $\tau \sim O(1)$, this requirement implies that

$$\delta t\,(\gamma L|\pmb{G}_0|)^2 \ll \frac{D}{L^2} \Rightarrow \delta t \ll \frac{D}{\gamma L^4|\pmb{G}_0|} \sim 10^{-4}\, ms \quad \text{(A15)}$$

APPENDIX B

The boundary condition at a thin permeable membrane involves conservation of mass flux, and this needs to be formulated in terms of the distribution functions and the membrane permeability. The derivation of the membrane boundary conditions is based on the formulation and results found in [42, 51] [52], so only the necessary background is given here. In order to facilitate the presentation, Figure B1 is drawn on the basis of the nomenclature and name convention in [51]. The variable distance from the lattice point in the intracellular region to the point at which the membrane cuts the lattice link is denoted by $\Delta\,\delta x$. So, Δ expresses the dimensionless distance between the internal node closest to the membrane and the membrane, and $0 < \Delta < 1$. Here we keep the LBM collision$\rightarrow$ streaming nomenclature we introduced in section 2, with the distributions denoted by $g_i \rightarrow \hat{g}_i \rightarrow g_i'$. As is the case with the external boundary conditions, each membrane boundary condition is enforced at the end of the LBM collision step, so extra subscripts are necessary to distinguish particle distributions based on the direction the "particles" move. Following [42], when the particle moves towards the membrane, we keep subscript i, and when they move away from the membrane, the subscript $\bar{\imath}$.
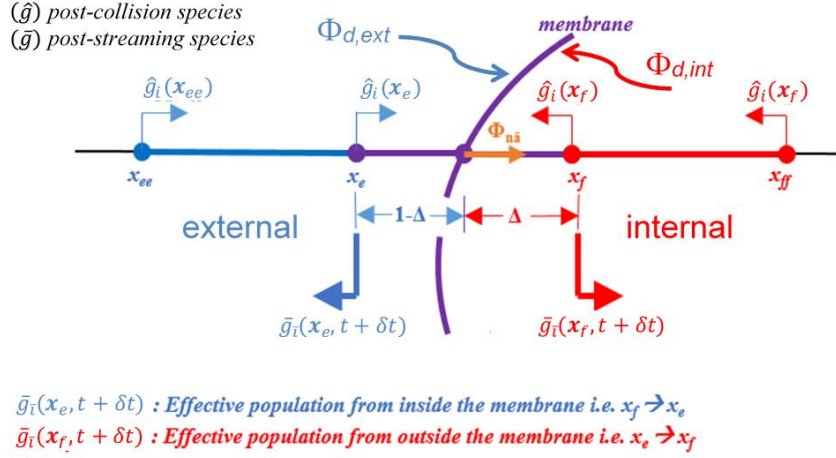
Figure B1. The particle probability distribution functions near the membrane interface and relationship to the local lattice.

We start by considering the interfacial conditions (28), which result in two relations expressed in terms of Dirichlet ($\Phi_d = M$) and Neumann ($\Phi_n = D\,\boldsymbol{n}\cdot\nabla M$) boundary conditions at either side the interface, with subscripts '*in*' and '*ex*' denoting the extra-and intra-cellular phase, respectively

$$\Phi_{n,ex} = -\Phi_{n,in}; \;\; \Phi_{n,in} = K\big(\Phi_{d,ex} - \Phi_{d,in}\big) \tag{B1}$$

The nomenclature of Li et al. [52] has been used in the sign convention of the Neumann boundary conditions above. We then consider the distribution functions representing particles towards the membrane in extra-and intra-cellular domains, denoted by $g_i'(\boldsymbol{x}_e, t)$ and $g_i'(\boldsymbol{x}_f, t)$, respectively. As in the main text, the reaction initialization step of $g_i'(\boldsymbol{x}_n, t) = \bar{g}_i(\boldsymbol{x}_n, t + \delta t)$ is implied. Enforcing the conditions (B1), we start from Eqs (14-17) of Li et al. [52] to derive

$$
\begin{aligned}
g'_{\bar{\imath}}(\boldsymbol{x}_f, t) =\; & A_1^f \hat{g}_i(\boldsymbol{x}_f), t + A_2^f \hat{g}_i(\boldsymbol{x}_{ff}, t) + A_3^f \hat{g}_{\bar{\imath}}(\boldsymbol{x}_f, t) + B_1^f \hat{g}_{\bar{\imath}}(\boldsymbol{x}_e, t) + B_2^f \hat{g}_{\bar{\imath}}(\boldsymbol{x}_{ee}, t) + \\
& B_3^f \hat{g}_i(\boldsymbol{x}_e, t) + C_1^f \hat{g}_i(\boldsymbol{x'}_f, t) + C_2^f \hat{g}_i(\boldsymbol{x'}_{ff}, t) + C_3^f \hat{g}_{\bar{\imath}}(\boldsymbol{x'}_f, t) + D_1^f \hat{g}_{\bar{\imath}}(\boldsymbol{x'}_e, t) + D_2^f \hat{g}_{\bar{\imath}}(\boldsymbol{x'}_{ee}, t) + \\
& D_3^f \hat{g}_i(\boldsymbol{x'}_e) \tag{B2a}
\end{aligned}
$$

$$
\begin{aligned}
g'_i(\boldsymbol{x}_e, t) =\; & A_1^e \hat{g}_{\bar{\imath}}(\boldsymbol{x}_e), t + A_2^e \hat{g}_{\bar{\imath}}(\boldsymbol{x}_{ee}, t) + A_3^e \hat{g}_i(\boldsymbol{x}_e, t) + B_1^e \hat{g}_i(\boldsymbol{x}_f, t) + B_2^e \hat{g}_i(\boldsymbol{x}_{ff}, t) + B_3^e \hat{g}_{\bar{\imath}}(\boldsymbol{x}_f, t) \\
& + C_1^e \hat{g}_{\bar{\imath}}(\boldsymbol{x'}_e, t) + C_2^e \hat{g}_{\bar{\imath}}(\boldsymbol{x'}_{ee}, t) + C_3^e \hat{g}_i(\boldsymbol{x'}_e, t) + D_1^e \hat{g}_i(\boldsymbol{x'}_f, t) + D_2^e \hat{g}_i(\boldsymbol{x'}_{ff}, t) \\
& + D_3^e \hat{g}_{\bar{\imath}}(\boldsymbol{x'}_f)
\end{aligned}
$$

$$\tag{B2b}$$

The subscripts '*e*' and '*ee*' in $\boldsymbol{x}$ denote lattice nodes immediately adjacent to the membrane in the extra-cellular domain, and the subscripts '*f*' and '*ff*' in the coefficients denote corresponding adjacent nodes in the intra-cellular domain. The superscripted $\boldsymbol{x'}$ refers to the extrapolated values from nodes within a respective domain for $\boldsymbol{x'}_e = \boldsymbol{x'}_f = \boldsymbol{x}_{membrane}$, $\boldsymbol{x'}_{ff} = \boldsymbol{x'}_f + \boldsymbol{e}_{\bar{\imath}}\,\delta t$, and $\boldsymbol{x'}_{ee} =$

$\mathbf{x'}_e + \mathbf{e}_{\bar{\imath}}\delta t$ where $\mathbf{e}_{\bar{\imath}}$ is in the direction orthogonal to the lattice direction (see Figure 1 in [51]for details). The coefficients in Eq (B2) are given below

$$A_i^f = \Big(c_{d4}c'_{n4}\cos\theta\,(c'_{n4}c^*_{d4}c_{ni}\epsilon_D\delta x\cos\theta + c'_{n4}\,c^*_{n4}\,c_{ni}K\,\delta x + c'_{d4}\,c^*_{n4}c_{ni}\,\epsilon_D\delta x\sin\theta)$$
$$+\ c_{n4}\big(\cos\theta\,c'_{n4}\,c^*_{d4}c_{di}\,(c'_{n4}\,K\,\delta x +\ c'_{d4}\epsilon_D\delta x\sin\theta)$$
$$+\ c'_{d4}c^*_{n4}c_{di}\sin\theta\,(2c'_{n4}\,K\,\delta x +\ c'_{d4}\epsilon_D\,\delta x\sin\theta)\big)\Big)\big/F$$

$$B_i^f = (c_{d4}c_{n4}c'^2_{n4}\,K\,\delta x\cos\theta\ (c^*_{ni} - c^*_{di}\,))/F$$

$$C_i^f = (c_{d4}c_{n4}c^*_{n4}c'_{n4}\,K\,\delta x\sin\theta\ (c'_{ni} - c'_{di}\,))/F$$

$$D_i^f = (c_{d4}c_{n4}\sin\theta\,(c'_{ni} - c'_{di})(c'_{n4}c^*_{d4}\,\epsilon_D\,\delta x\cos\theta +\ c'_{n4}c^*_{n4}\,K\,\delta x +\ c'_{d4}c^*_{n4}\,\epsilon_D\,\delta x\sin\theta))/F$$

$$(B3a)$$

and

$$A_i^e = \Big(c_{d4}c'_{n4}\cos\theta\,(c'_{n4}c^*_{d4}c^*_{ni}\epsilon_D\delta x\cos\theta + c'_{n4}\,c^*_{n4}\,c^*_{di}K\,\delta x + c'_{d4}\,c^*_{n4}c^*_{di}\,\epsilon_D\delta x\sin\theta)$$
$$+\ c_{n4}\big(\cos\theta\,c'_{n4}\,c^*_{d4}c^*_{ni}\,(c'_{n4}\,K\,\delta x +\ c'_{d4}\epsilon_D\delta x\sin\theta)$$
$$+\ c'_{d4}c^*_{n4}c^*_{ni}\sin\theta\,(2c'_{n4}\,K\,\delta x +\ c'_{d4}\epsilon_D\,\delta x\sin\theta)\big)\Big)\big/F$$

$$B_i^e = (c^*_{d4}c^*_{n4}c'^2_{n4}\,K\,\delta x\cos\theta\ (c_{ni} - c_{di}\,))/F$$

$$C_i^e = (c^*_{d4}c_{n4}c^*_{n4}c'_{n4}\,K\,\delta x\sin\theta\ (c'_{ni} - c'_{di}\,))/F$$

$$D_i^e = (c^*_{d4}c^*_{n4}\sin\theta\,(c'_{ni} - c'_{di})(c'_{n4}c_{d4}\,\epsilon_D\,\delta x\cos\theta +\ c'_{n4}c_{n4}\,K\,\delta x +\ c'_{d4}c_{n4}\,\epsilon_D\,\delta x\sin\theta))/F$$

$$(B3b)$$

With

$$F = \Big(c_{d4}\,c'_{n4}\cos\theta\,(\cos\theta\,c'_{n4}c^*_{d4}\,\epsilon_D dx + c'_{n4}\,c^*_{n4}\,K\,\delta x + c'_{d4}\,c^*_{n4}\,\epsilon_D\delta x\sin\theta)$$
$$+\ c_{n4}\big(\cos\theta\,c'_{n4}\,c^*_{d4}\,(c'_{n4}\,K\,\delta x +\ c'_{d4}\epsilon_D\delta x\sin\theta)$$
$$+\ c'_{d4}c^*_{n4}\sin\theta\,(2c'_{n4}\,K\,\delta x +\ c'_{d4}\epsilon_D\,\delta x\sin\theta)\big)\Big)$$

$$(B3c)$$

Here θ is the angle between the normal to the membrane and lattice direction i while the coefficients c_{di} and c_{ni} are the coefficients of the Dirichlet and Neumann boundary conditions derived in [53] for a lattice membrane distance of Δ, c^*_{di} and c^*_{ni} are the same coefficients for the extracellular fraction $\Delta^* = (1 - \Delta)$, and c'_{di} and c'_{ni} are the coefficients for $\Delta = 0$. If the boundary is perpendicular to the lattice then $\Phi_n = \Phi_{n,i}$, and this means the angle between the normal to the membrane and the lattice direction i is $\theta = 0$, yielding a simplified version of the coefficients (cf. Figure B1)

$$A_i^f = (c_{d4}c^*_{d4}c_{ni}\epsilon_D\delta x + (c_{d4}c^*_{n4}\,c_{ni} + c_{n4}c^*_{d4}c_{di})K\,\delta x)/F$$

$$B_i^f = (c_{d4} c_{n4} \; (c_{ni}^* - c_{di}^*) \; K \; \delta x)/F$$
$$C_i^f = D_i^f = 0$$

$$(B4a)$$

and
$$A_i^e = (c_{d4} c_{d4}^* c_{ni}^* \epsilon_D \delta x + (c_{d4} c_{n4}^* c_{di}^* + c_{n4} \; c_{d4}^* c_{ni}^*) K \; \delta x)/F$$
$$B_i^e = (c_{d4}^* c_{n4}^* (c_{ni} - c_{di}) \; K \; \delta x)/F$$
$$C_i^e = D_i^e = 0$$

$$(B4b)$$

With
$$F = c_{d4} \; c_{d4}^* \; \epsilon_D \delta x + (c_{d4} \; c_{n4}^* + c_{n4} c_{d4}^*) K \; \delta x$$

$$(B4c)$$

Finally, setting $\Delta = 0.5$ and choosing $c_{d1} = 2(\Delta - 1)$, with the other coefficients described in [53], the coefficients given by Equations $(B4)$ further reduce to

$$A_1^f = \frac{P}{1+P}$$
$$B_1^f = \frac{1}{1+P}$$
$$A_1^e = \frac{P}{1+P}$$
$$B_1^e = \frac{1}{1+P}$$

$$(B5)$$

where $P = \frac{\epsilon_D}{K} \frac{\delta x}{\delta t}$ and all other coefficients are zero. Recall that $\epsilon_D = 1/3$ for D2Q5.

REFERENCES

[1] P.T. Callaghan, Principles of Nuclear Magnetic Resonance Microscopy, Oxford University Press, New York, 1993.

[2] G.G. Cleveland, D.C. Chang, C.F. Hazlewood, H.E. Rorschach, Nuclear magnetic resonance measurement of skeletal muscle anisotropy of the diffusion coefficient of the intracellular water, Biophys. J., 16 (1976) 1043-1053.

[3] S.T. Kinsey, B.R. Locke, B. Penke, T.S. Moerland, Diffusional anisotropy is induced by subcellular barriers in skeletal muscle, Nmr in Biomedicine, 12 (1999) 1-7.

[4] B.M. Damon, Z. Ding, A.W. Anderson, A.S. Freyer, J.C. Gore, Validation of Diffusion Tensor MRI-based Muscle Fiber Tracking, Magn Reson. Med., 48 (2002) 97-104.

[5] S. Sinha, U. Sinha, V.R. Edgerton, In vivo diffusion tensor imaging of the human calf muscle, Journal of Magnetic Resonance Imaging, 24 (2006) 182-190.

[6] D.C. Karampinos, K.F. King, B.P. Sutton, J.G. Georgiadis, Myofiber Ellipticity as an Explanation for Transverse Asymmetry of Skeletal Muscle Diffusion MRI in vivo Signal, Annals of Biomedical Engineering, 37 (2009) 2532-2546.

[7] D.C. Karampinos, S. Banerjee, K.F. King, T.M. Link, S. Majumdar, Considerations in high-resolution skeletal muscle diffusion tensor imaging using single-shot echo planar imaging with stimulated-echo preparation and sensitivity encoding, Nmr in Biomedicine, 25 (2012) 766-778.

[8] B.M. Damon, M. Froeling, A.K.W. Buck, J. Oudeman, Z.H. Ding, A.J. Nederveen, E.C. Bush, G.J. Strijkersh, Skeletal muscle diffusion tensor-MRI fiber tracking: rationale, data acquisition and analysis methods, applications and future directions, Nmr in Biomedicine, 30 (2017) e3563.

[9] D. Le Bihan, H. Johansen-Berg, Diffusion MRI at 25: Exploring brain tissue structure and function, Neuroimage, 61 (2012) 324-341.

[10] K. Setsompop, R. Kimmlingen, E. Eberlein, T. Witzel, J. Cohen-Adad, J.A. McNab, B. Keil, M.D. Tisdall, P. Hoecht, P. Dietz, S.F. Cauley, V. Tountcheva, V. Matschl, V.H. Lenz, K. Heberlein, A. Potthast, H. Thein, J. Van Horn, A. Toga, F. Schmitt, D. Lehne, B.R. Rosen, V. Wedeen, L.L. Wald, Pushing the limits of in vivo diffusion MRI for the Human Connectome Project, Neuroimage, 80 (2013) 220-233.

[11] D.G. Norris, The effects of microscopic tissue parameters on the diffusion weighted magnetic resonance imaging experiment, Nmr in Biomedicine, 14 (2001) 77-93.

[12] V.G. Kiselev, Fundamentals of diffusion MRI physics, Nmr in Biomedicine, 30 (2017) e3602.

[13] M.G. Hall, C.A. Clark, Diffusion in hierarchical systems: A simulation study in models of healthy and diseased muscle tissue, Magnetic Resonance in Medicine, 78 (2017) 1187-1198.

[14] B.M. Damon, Effects of image noise in muscle diffusion tensor (DT)-MRI assessed using numerical simulations, Magnetic Resonance in Medicine, 60 (2008) 934-944.

[15] D. Hernando, D.C. Karampinos, K.F. King, J.P. Haldar, S. Majumdar, J.G. Georgiadis, Z.P. Liang, Removal of olefinic fat chemical shift artifact in diffusion MRI, Magn Reson Med, 65 (2011) 692-701.

[16] D.S. Grebenkov, NMR survey of reflected Brownian motion, Reviews of Modern Physics, 79 (2007) 1077-1137.

[17] E.E. Sigmund, D.S. Novikov, D.B. Sui, O. Ukpebor, S. Baete, J.S. Babb, K.C. Liu, T. Feiweier, J. Kwon, K. McGorty, J. Bencardino, E. Fieremans, Time-dependent diffusion in skeletal muscle with the random permeable barrier model (RPBM): application to normal

controls and chronic exertional compartment syndrome patients, Nmr in Biomedicine, 27 (2014) 519-528.

[18] E. Fieremans, G. Lemberskiy, J. Veraart, E.E. Sigmund, S. Gyftopoulos, D.S. Novikov, In vivo measurement of membrane permeability and myofiber size in human muscle using time-dependent diffusion tensor imaging and the random permeable barrier model, Nmr in Biomedicine, 30 (2017) e3612.

[19] D.S. Novikov, V.G. Kiselev, Effective medium theory of a diffusion-weighted signal, Nmr in Biomedicine, 23 (2010) 682-697.

[20] H. Torrey, Bloch equations with diffusion terms Physical Review, 104 (1956) 563-565.

[21] I.O. Jelescu, M.D. Budde, Design and Validation of Diffusion MRI Models of White Matter, Frontiers in Physics, 5 (2017) 61.

[22] R.L. Magin, O. Abdullah, D. Baleanu, X.H.J. Zhou, Anomalous diffusion expressed through fractional order differential operators in the Bloch-Torrey equation, Journal of Magnetic Resonance, 190 (2008) 255-270.

[23] C. Ionescu, A. Lopes, D. Copot, J.A.T. Machado, J.H.T. Bates, The role of fractional calculus in modeling biological phenomena: A review, Commun. Nonlinear Sci. Numer. Simul., 51 (2017) 141-159.

[24] A. Szafer, J. Zhong, J.C. Gore, Theoretical model for water diffusion in tissues, Magn. Reson. Med., 33 (1995) 697-612.

[25] G.T. Balls, L.R. Frank, A Simulation Environment for Diffusion Weighted MR Experiments in Complex Media, Magnetic Resonance in Medicine, 62 (2009) 771-778.

[26] E. Fieremans, D.S. Novikov, J.H. Jensen, J.A. Helpern, Monte Carlo study of a two-compartment exchange model of diffusion, Nmr in Biomedicine, 23 (2010) 711-724.

[27] G.T. Baxter, L.R. Frank, A computational model for diffusion weighted imaging of myelinated white matter, Neuroimage, 75 (2013) 204-212.

[28] C.H. Yeh, B. Schmitt, D. Le Bihan, J.R. Li-Schlittgen, C.P. Lin, C. Poupon, Diffusion Microscopist Simulator: A General Monte Carlo Simulation System for Diffusion Magnetic Resonance Imaging, Plos One, 8 (2013) 0076626.

[29] D.B. Berry, B. Regner, V. Galinsky, S.R. Ward, L.R. Frank, Relationships Between Tissue Microstructure and the Diffusion Tensor in Simulated Skeletal Muscle, Magnetic Resonance in Medicine, 80 (2018) 317-329.

[30] C.L. Chin, F.W. Wehrli, S.N. Hwang, M. Takahashi, D.B. Hackney, Biexponential diffusion attenuation in the rat spinal cord: Computer simulations based on anatomic images of axonal architecture, Magnetic Resonance in Medicine, 47 (2002) 455-460.

[31] S.N. Hwang, C.L. Chin, F.W. Wehrli, D.B. Hackney, An image-based finite difference model for simulating restricted diffusion, Magnetic Resonance in Medicine, 50 (2003) 373-382.

[32] J.Z. Xu, M.D. Does, J.C. Gore, Numerical study of water diffusion in biological tissues using an improved finite difference method, Physics in Medicine and Biology, 52 (2007) N111-N126.

[33] G. Russell, K.D. Harkins, T.W. Secomb, J.P. Galons, T.P. Trouard, A finite difference method with periodic boundary conditions for simulations of diffusion-weighted magnetic resonance experiments in tissue, Physics in Medicine and Biology, 57 (2012) N35-N46.

[34] D.V. Nguyen, J.-R. Li, D. Grebenkov, D. Le Bihan, A finite elements method to solve the Bloch–Torrey equation applied to diffusion magnetic resonance imaging, J. Comput. Phys., 263 (2014) 283-302.

[35] L. Beltrachini, Z.A. Taylor, A.F. Frangi, A parametric finite element solution of the generalised Bloch-Torrey equation for arbitrary domains, Journal of Magnetic Resonance, 259 (2015) 126-134.

[36] V.-D. Nguyen, J. Jansson, J. Hoffman, J.-R. Li, A partition of unity finite element method for computational diffusion MRI, J. Comput. Phys., 375 (2018) 271-290.

[37] J.R. Li, D. Calhoun, C. Poupon, D. Le Bihan, Numerical simulation of diffusion MRI signals using an adaptive time-stepping method, Physics in Medicine and Biology, 59 (2014) 441-454.

[38] M.G. Hall, D.C. Alexander, Convergence and Parameter Choice for Monte-Carlo Simulations of Diffusion MRI, IEEE Transactions on Medical Imaging, 28 (2009) 1354-1364.

[39] M.V. Chubynsky, G.W. Slater, Optimizing the accuracy of lattice Monte Carlo algorithms for simulating diffusion, Phys. Rev. E, 85 (2012) 016709.

[40] D.R. Noble, S.Y. Chen, J.G. Georgiadis, R.O. Buckius, A Consistent Hydrodynamic Boundary Condition for the Lattice Boltzmann Method, Physics of Fluids, 7 (1995) 203-209.

[41] M.A. Gallivan, D.R. Noble, J.G. Georgiadis, R.O. Buckius, An evaluation of the bounce-back boundary condition for lattice Boltzmann simulations, International Journal for Numerical Methods in Fluids, 25 (1997) 249-263.

[42] L.K. Li, R.W. Mei, J.F. Klausner, Boundary conditions for thermal lattice Boltzmann equation method, J. Comput. Phys., 237 (2013) 366-395.

[43] L.Q. Zhang, S.L. Yang, Z. Zeng, J.W. Chew, Consistent second-order boundary implementations for convection-diffusion lattice Boltzmann method, Phys. Rev. E, 97 (2018) 20.

[44] Y. Zhao, Lattice boltzmann based PDE solver on the GPU, Visual Comput., 24 (2008) 323-333.

[45] J.R. Clausen, D.A. Reasor, C.K. Aidun, Parallel performance of a lattice-Boltzmann/finite element cellular blood flow solver on the IBM Blue Gene/P architecture, Computer Physics Communications, 181 (2010) 1013-1020.

[46] J. Campos, R.S. Oliveira, R.W. dos Santos, B.M. Rocha, Lattice Boltzmann method for parallel simulations of cardiac electrophysiology using GPUs, Journal of Computational and Applied Mathematics, 295 (2016) 70-82.

[47] A. Hiorth, U.H.A. Lad, S. Evje, S.M. Skjaeveland, A lattice Boltzmann-BGK algorithm for a diffusion equation with Robin boundary condition-application to NMR relaxation, International Journal for Numerical Methods in Fluids, 59 (2009) 405-421.

[48] D. Alemani, B. Chopard, J. Galceran, J. Buffle, LBGK method coupled to time splitting technique for solving reaction-diffusion processes in complex systems, Physical Chemistry Chemical Physics, 7 (2005) 3331-3341.

[49] L. Li, R. Mei, J.F. Klausner, Lattice Boltzmann models for the convection-diffusion equation: D2Q5 vs D2Q9, Int. J. Heat Mass Transf., 108 (2017) 41-62.

[50] C. Huber, B. Chopard, M. Manga, A lattice Boltzmann model for coupled diffusion, J. Comput. Phys., 229 (2010) 7956-7976.

[51] K. Guo, L. Li, G. Xiao, N. AuYeung, R. Mei, Lattice Boltzmann method for conjugate heat and mass transfer with interfacial jump conditions, Int. J. Heat Mass Transf., 88 (2015) 306-322.

[52] L.K. Li, C. Chen, R.W. Mei, J.F. Klausner, Conjugate heat and mass transfer in the lattice Boltzmann equation method, Phys. Rev. E, 89 (2014) 21.

[53] V. Kenkre, E. Fukushima, D. Sheltraw, Simple solutions of the Torrey–Bloch equations in the NMR study of molecular diffusion, Journal of Magnetic Resonance, 128 (1997) 62-69.

[54] O. Soderman, B. Jonsson, Restricted Diffusion in Cylindrical Geometry, J. Magn. Reson. Ser. A, 117 (1995) 94-97.

[55] W.T. Perrins, D.R. McKenzie, R.C. McPhedran, Transport Properties of Regular Arrays of Cylinders, Proceedings of the Royal Society of London Series a-Mathematical Physical and Engineering Sciences, 369 (1979) 207-225.

[56] G.J. Stanisz, A. Szafer, G.A.W. abd R. M. Henkelman, An analytical model of restricted diffusion in bovine optic nerve, Magn. Reson. Med., 37 (1997) 103-111.

[57] M.Y. Wang, J.G. Georgiadis, Conjugate forced convection in crossflow over a cylinder array with volumetric heating, Int. J. Heat Mass Transf., 39 (1996) 1351-1361.

[58] M.Y. Wang, J.G. Georgiadis, Parallel computation of forced convection using domain decomposition, Numerical Heat Transfer Part B-Fundamentals, 20 (1991) 41-59.

[59] J. Towns, T. Cockerill, M. Dahan, I. Foster, K. Gaither, A. Grimshaw, V. Hazlewood, S. Lathrop, D. Lifka, G.D. Peterson, XSEDE: accelerating scientific discovery, Computing in Science & Engineering, 16 (2014) 62-74.

[60] T. Kruger, H. Kusumaatmaja, A. Kuzmin, O. Shardt, G. Silva, E.M. Viggen, Lattice Boltzmann Method: Principles and Practice, in: Lattice Boltzmann Method: Principles and Practice, 2017, pp. 1-694.

[61] D.J. Holdych, D.R. Noble, J.G. Georgiadis, R.O. Buckius, Truncation error analysis of lattice Boltzmann methods, J. Comput. Phys., 193 (2004) 595-619.

[62] S.G. Ayodele, F. Varnik, D. Raabe, Lattice Boltzmann study of pattern formation in reaction-diffusion systems, Phys. Rev. E, 83 (2011) 016702.

[63] D. Wolfgladrow, A Lattice Boltzmann Equation for Diffusion, Journal of Statistical Physics, 79 (1995) 1023-1032.

[64] I. Ginzburg, Equilibrium-type and link-type lattice Boltzmann models for generic advection and anisotropic-dispersion equation, Adv. Water Resour., 28 (2005) 1171-1195.

[65] H. Yoshida, M. Nagaoka, Multiple-relaxation-time lattice Boltzmann model for the convection and anisotropic diffusion equation, J. Comput. Phys., 229 (2010) 7774-7795.

[66] V. Aho, K. Mattila, T. Kuhn, P. Kekalainen, O. Pulkkinen, R.B. Minussi, M. Vihinen-Ranta, J. Timonen, Diffusion through thin membranes: Modeling across scales, Phys. Rev. E, 93 (2016) 14.

[67] D.J. Holdych, J.G. Georgiadis, R.O. Buckius, Migration of a van der Waals bubble: Lattice Boltzmann formulation, Physics of Fluids, 13 (2001) 817-825.

[68] J.G. Georgiadis, D. Noble, M.R. Uchanski, R.O. Buckius, Tortuous micro-flow in large disordered packed beds, ASME J. Fluids Eng., 118 (1996) 434-436.

[69] K. Jurczuk, M. Kretowski, J.J. Bellanger, P.A. Eliat, H. Saint-Jalmes, J. Bezy-Wendling, Computational modeling of MR flow imaging by the lattice Boltzmann method and Bloch equation, Magnetic Resonance Imaging, 31 (2013) 1163-1173.

[70] S. Khirevich, I. Ginzburg, U. Tallarek, Coarse- and fine-grid numerical behavior of MRT/TRT lattice-Boltzmann schemes in regular and random sphere packings, J. Comput. Phys., 281 (2015) 708-742.

[71] T. Kuhn, T.O. Ihalainen, J. Hyvaluoma, N. Dross, S.F. Willman, J. Langowski, M. Vihinen-Ranta, J. Timonen, Protein Diffusion in Mammalian Cell Cytoplasm, Plos One, 6 (2011).

[72] J.G. Zhou, P.M. Haygarth, P.J.A. Withers, C.J.A. Macleod, P.D. Falloon, K.J. Beven, M.C. Ockenden, K.J. Forber, M.J. Hollaway, R. Evans, A.L. Collins, K.M. Hiscock, C. Wearing, R. Kahana, M.L.V. Velez, Lattice Boltzmann method for the fractional advection-diffusion equation, Phys. Rev. E, 93 (2016) 9.